# STARS

2011

# Variational Embedded Solitons, And Traveling Wavetrains Generated By Generalized Hopf Bifurcations, In Some Nlpde Systems

Todd Blanton Smith
*University of Central Florida*

# Variational Embedded Solitons, and Traveling Wavetrains Generated by Generalized Hopf Bifurcations, in some NLPDE Systems

by

## Todd Blanton Smith
B.S. Auburn University, 2004
M.S. University of Central Florida, 2007

A dissertation submitted in partial fulfillment of the requirements
for the degree of Doctor of Philosophy
in the Department of Mathematics
in the College of Sciences
at the University of Central Florida
Orlando, Florida

Spring Term
2011

Major Professor: Roy S. Choudhury

## Abstract

In this Ph.D. thesis, we study regular and embedded solitons and generalized and degenerate Hopf bifurcations. These two areas of work are seperate and independent from each other. First, variational methods are employed to generate families of both regular and embedded solitary wave solutions for a generalized Pochhammer PDE and a generalized microstructure PDE that are currently of great interest. The technique for obtaining the embedded solitons incorporates several recent generalizations of the usual variational technique and is thus topical in itself. One unusual feature of the solitary waves derived here is that we are able to obtain them in analytical form (within the family of the trial functions). Thus, the residual is calculated, showing the accuracy of the resulting solitary waves. Given the importance of solitary wave solutions in wave dynamics and information propagation in nonlinear PDEs, as well as the fact that only the parameter regimes for the existence of solitary waves had previously been analyzed for the microstructure PDE considered here, the results obtained here are both new and timely.

Second, we consider generalized and degenerate Hopf bifurcations in three different models: i. a predator-prey model with general predator death rate and prey birth rate terms, ii. a laser-diode system, and iii. traveling-wave solutions of two-species predator-prey/reaction-diffusion equations with arbitrary nonlinear/reaction terms. For specific choices of the nonlinear terms, the quasi-periodic orbit in the post-bifurcation regime is constructed for each system using the method of multiple scales, and its stability is analyzed via the corresponding normal form obtained by reducing the system down to the center manifold. The resulting predictions for the post-bifurcation dynamics provide an organizing framework for the variety of possible behaviors. These predictions are verified and supplemented by numerical simulations, including the computation of power spectra, autocorrelation functions, and fractal dimensions as appropriate for the periodic and quasiperiodic attractors, attractors at infinity, as well as bounded chaotic attractors obtained in various cases. The dynamics obtained in the three systems is contrasted and explained on the basis of the bifurcations occurring in each. For instance, while the two predator-prey models yield a variety of behaviors in the post-bifurcation regime, the laser-diode evinces extremely stable quasiperiodic solutions over a wide range of parameters, which is very desirable for robust operation of the system in oscillator mode.

*To my family, for their support.*

## Acknowledgments

# TABLE OF CONTENTS

# PART IV  DYNAMICAL CONSEQUENCES OF DOUBLE HOPF BIFURCATIONS                    94

# LIST OF FIGURES

# Part I

# INTRODUCTION

# CHAPTER 1
# INTRODUCTION

## 1.1   Variational Methods for Regular and Embedded Solitons

In Part II of this thesis, variational methods are employed to generate families of both regular and embedded solitary wave solutions for a generalized Pochhammer PDE and a generalized microstructure PDE that are of great interest. The technique for obtaining the embedded solitons incorporates several recent generalizations of the usual variational technique and is thus topical in itself. One unusual feature of the solitary waves derived here is that we are able to obtain them in analytical form (within the family of the trial functions). Thus, the residual is calculated, showing the accuracy of the resulting solitary waves. Given the importance of solitary wave solutions in wave dynamics and information propagation in nonlinear PDEs, as well as the fact that only the parameter regimes for the existence of solitary waves had previously been analyzed for the microstructure PDE considered here, the results obtained here are both new and timely.

## 1.2 Bifurcation of Limit Cycles

In the rest of the dissertation we study a seperate and independent problem. Many physical systems exhibit self-sustaining oscillatory behavior with no external periodic forcing; for example, a beating heart, a vibration in an airplane wing, or the interacting populations of several species. This type of behavior is modeled in by limit cycle solutions of the corresponding nonlinear dynamical systems. A limit cycle is an isolated periodic orbit, meaning that no other periodic orbits exist sufficiently close to it in state space. Every nearby trajectory approaches the orbit as $t \to \infty$ or as $t \to -\infty$. Limit cycles are pervasive throughout physics, biology, chemistry and economics, and limit cycle theory has consequently grown into a popular and interesting field of research.

From the point of view of dynamical system theory, limit cycles are generated through four kinds of bifurcations: multiple Hopf bifurcations from a center or focus, separatrix cycle bifurcations from homoclinic or heteroclinic orbits, global center bifurcations from a periodic annulus, and limit cycle bifurcations from multiple limit cycles. Bifurcations involving separatricies or global bifurcations are within the realm of global bifurcation theory and are usually studied with theories such as Poincaré-Pontrayagin-Andronov or higher-order Melnikov function analysis. Limit cycles bi-

furcated from a focus, center, or other limit cycles are called local bifurcations and are studied by normal form and other local bifurcation theories [1, 2].

While there have been a very large number of studies of regular Hopf bifurcations, generalized and degenerate Hopf bifurcations are far less widely studied. Among recent comprehensive treatments, we may list the monograph by Huseyin [3], the thesis by Planeaux [4], and the recent review by Yu [5]. The first named is reasonably comprehensive at the analytical end but employs the little-used generalized Harmonic Balance asymptotic analysis technique. By contrast, [4] is a comprehensive numerical analysis in the context of chemical reactor dynamics. Ref. [5] uses a mix of analytic techniques, together with limited numerical simulations, to consider the dynamics resulting from generalized and degenerate Hopf bifurcations.

In Part III of this thesis, we consider generalized and degenerate Hopf bifurcations comprehensively, using the established and widely-accepted multiple-scales asymptotic technique for the analysis, as well as a variety of numerical solutions and diagnostics. To operate on a broad platform, we consider three different models: i. a predator-prey model with general predator death rate and prey birth rate terms, ii. a laser-diode system, and iii. traveling-wave solutions of two-species predator-prey/ reaction-diffusion equations with arbitrary nonlinear/reaction terms.

For specific choices of the nonlinear terms, the quasi-periodic orbit in the post-bifurcation regime is constructed for each system with the method of multiple-scales using the following steps. After expansions in several progressively slower time scales are substituted into each variable and parameter, equations are separated by time scales. Motion on each time scale can be represented by a differential operator for each equation, and each operator is the same at each scale. These general operators can be combined algebraically to eliminate all but one variable, giving a higher order composite differential operator that holds information from all the general first order differential equations for any time scale. This process creates a homogeneous equation for the first time scale (we assume that appropriate changes of variable have already been made to translate the system into one with a fixed point at the origin). Sources for the other equations at slower time scales are only functions of equations with faster time scales.

The composite operator can be solved one scale at a time. The first order (fastest time scale) operator is homogeneous and so an ansatz can be imposed to give a solution with the desired behavior. In our case we chose the ansatz to be a sum of exponential functions. The same equations that we used to create the composite operator before can now be used to find solutions for the other first order space variables based on our chosen ansatz.

Now that the first order operators are known, they can be plugged into the second order equation's source to fully determine it. If any term in the newly determined source satisfies the homogeneous operator, then, following a standard undetermined coefficients approach, a particular solution would involve a multiple of that term multiplied by the time variable to at least the first power. This would be unacceptable, as it would cause an otherwise oscillating term to have an amplitude that approaches infinity with time. The types of motion we desire need to be localized in space near some fixed point. The elimination of these secular terms is a necessity that we use to determine the second order normal form, which is the system of differential equations in the coefficients of each term of the second order ansatz. This process is repeated as many times as necessary. For our three-dimensional system, we found the required normal form after eliminating secular terms in the second order source. For our four-dimensional system, the normal form was found after eliminating secular terms in the third order source.

Once the normal form is found, standard fixed point analysis allows us to find appropriate parameter values, that when plugged into the first order ansatz, yields the post-generalized Hopf periodic orbits. Their stability is usually analyzed with standard phase plane analysis. However, in our two systems, the standard analysis fails since the eigenvalue of the Jacobian of the normal form at the origin is

zero. These predictions are replaced and supplemented by numerical simulations, including the computation of power spectra, autocorrelation functions, and fractal dimensions as appropriate for the periodic and quasiperiodic attractors, attractors at infinity, as well as bounded chaotic attractors obtained in various cases. The resulting post-bifurcation dynamics provide an organizing framework for the variety of possible behaviors. The dynamics obtained in the three systems is contrasted and explained on the basis of the bifurcations occurring in each. For instance, while the two predator-prey models yield a variety of behaviors in the post-bifurcation regime, the laser-diode evinces extremely stable quasiperiodic solutions over a wide range of parameters, which is very desirable for robust operation of the system in oscillator mode.

Next, secondary bifurcations are investigated. Static bifurcations of a periodic orbit can cause quasiperiodic behavior and a secondary Hopf bifurcation of a periodic orbit can create a three-dimensional torus in space. Both of these scenarios may lead to chaotic motion under further parameter variation. This work will lay out exact regions of parameter space for which changes in second order deviations of two particular parameters lead to each of the aforementioned system behaviors.

## 1.3   Organization of the Dissertation

The remainder of this dissertation is organized as follows. In Part II (Chapters 2-3), we use a Rayleigh-Ritz variational technique to create regular solitons in two widely used PDEs: a generalized Pochhammer-Chree PDE and a generalized microstructure PDE. Then we extend the method in a way which incorporates several recent generalizations of the usual variational technique to obtain analytical expressions for embedded solitons. In part III (Chapters 4-5), we investigate the effects of second-order parameter deviations on the dynamics of three systems whose parameters satisfy conditions for the existence of a generalized Hopf bifurcation. In Chapter 4 we examine a laser diode system, and in Chapter 5 we examine a predator-prey model with delay terms. In Part IV (Chapter 6), we examine nonlinear dynamics resulting from double-Hopf bifurcations in a fourth-order population model.

**Part II**

# VARIATIONAL METHODS FOR REGULAR AND EMBEDDED SOLITONS

# CHAPTER 2
# REGULAR AND EMBEDDED SOLITONS IN A GENERALIZED POCHHAMMER PDE

## 2.1   Abstract

In this chapter, variational methods are employed to generate families of both regular and embedded solitary wave solutions for a generalized Pochhammer PDE that of great interest. The technique for obtaining the embedded solitons incorporates several recent generalizations of the usual variational technique and is thus topical in itself. One unusual feature of the solitary waves derived here is that we are able to obtain them in analytical form (within the family of the trial functions) and calculate their residuals. Given the importance of solitary wave solutions in wave dynamics and information propagation in nonlinear PDEs, as well as the fact that only the parameter regimes for the existence of solitary waves had previously been analyzed for the microstructure PDE considered here, the results obtained here are both new and timely.

## 2.2   Introduction

The propagation of longitudinal deformation waves in elastic rods is governed [6–8] by the Generalized Pochammer-Chree Equation:

$$u_{tt} - u_{ttxx} - (\alpha_1 u + \alpha_2 u^2 + \alpha_3 u^3)_{xx} = 0 \qquad (2.2.1)$$

Here, $\alpha_1$, $\alpha_2$, and $\alpha_3$ are dimensionless parameters, and $x$ and $t$ denote space and time coordinates, respectively.

References [6–8] include derivations and applications of these equations in various fields. In addition, motivated by experimental and numerical results, there are derivations of special families of solitary wave solutions by the extended $Tanh$ method [6], and other ansatzen [8]. These extend earlier solitary wave solutions given by Bogolubsky [9] and Clarkson et al. [10] for special cases of (2.2.1). In addition, [7] generalizes the existence results in [11] for solitary waves of (2.2.1).

An analytical method for finding regular and embedded solitons with a variational approach was given in [12]. The method for finding regular solitary waves variationally is long-standing and widely used. By contrast, that for finding the so-called embedded solitons is of very recent vintage. The embedded solitons are embedded both in the continuous spectrum in spectral space and in a continuum of so-called delocalized solitary waves with oscillatory tails of exponentially small amplitude. In

11

this chapter, we shall construct regular solitary waves of (2.2.1) variationally and follow the extensions of that method in [12] to construct embedded soliton families of (2.2.1).

Towards that end and since both types of solitary wave solutions will be traveling-waves, we first derive the traveling-wave reduced ODE corresponding to (2.2.1). First, we transform to the traveling-wave variable $z = x - ct$. The derivatives are transformed as below.

$$\frac{\mathrm{d}}{\mathrm{d}x} = \frac{\mathrm{d}}{\mathrm{d}z}\frac{\mathrm{d}z}{\mathrm{d}x} = \frac{\mathrm{d}}{\mathrm{d}z} \tag{2.2.2}$$

$$\frac{\mathrm{d}}{\mathrm{d}t} = \frac{\mathrm{d}}{\mathrm{d}z}\frac{\mathrm{d}z}{\mathrm{d}t} = c\frac{\mathrm{d}}{\mathrm{d}z} \tag{2.2.3}$$

Now the PDE is an ODE:

$$c^2 u_{zz} - c^2 u_{zzzz} - (\alpha_1 u + \alpha_2 u^2 + \alpha_3 u^3)_{zz} = 0 \tag{2.2.4}$$

After and integrating twice, we have the following ODE (2.2.5) governing 1-D longitudinal wave propagation, with parameters defined by (2.2.6). Boundary conditions are not taken into account. The solitons constructed for this equation correspond to homoclinic orbits.

$$(1 - a_1)u - a_2 u^2 - a_3 u^3 - u'' = 0 \tag{2.2.5}$$

$$a_i = \alpha_i/c^2, \qquad 1 \le i \le 3 \tag{2.2.6}$$

## 2.3 The linear spectrum

As mentioned above, embedded solitary waves exist within a continuum of delocalized solitary waves with oscillating tails, as opposed to the exponentially decaying tails of regular solitary waves. This distinction may be used, together with an analysis of the tail region, to identify the disjoint parameter regimes where each of the two types of solitary waves may exist.

First, we perform a Taylor analysis of the tail of the potential soliton to find parameter regions where regular or embedded solitons could exist. Regular solitary waves have a vanishing amplitude for large $|z|$, and embedded solitary waves will have oscillating tails. These two behaviors can be modeled by an exponential function with either a negative or imaginary argument. We use the simple exponential ansatz below.

$$\phi = A \exp(\lambda z). \tag{2.3.1}$$

This is plugged into the linearized ODE to find the behavior of the tails. Note that the solution and its derivatives are very small in the tail for both types of solitary wave solutions. This is true even for embedded solitary waves since the tail oscillations have exponentially small amplitudes. Hence, the linearized ODE may be used.

$$(1 - a_1)Ae^{\lambda z} - \lambda^2 Ae^{\lambda z} = 0 \tag{2.3.2}$$

Solveing for $\lambda$ reveals the eigenvalues

$$\lambda = \pm\sqrt{1 - a_1}. \tag{2.3.3}$$

Therefore, parameter regimes with $a_1 < 1$ correspond to regular solitary waves with exponentially decaying tails, while parameter regimes with $a_1 > 1$ support embedded solitons with oscillatory tails.

## 2.4  Variational formulation

### 2.4.1  The variational approximation for regular solitons

The procedure for constructing regular solitary waves with exponentially decaying tails is well-known. It is widely employed in many areas of applied mathematics and goes by the name of the Rayleigh-Ritz method. In this section, we shall employ it to construct regular solitary waves of (2.2.5).

For this purpose, we first require the corresponding Lagrangian. The Lagrangian having equation (2.2.5) as its Euler-Lagrange equation is

$$(1 - a_1)u^2/2 - a_2u^3/3 - a_3u^4/4 - u_{zz}u/2 \tag{2.4.1}$$

This may be found by comparison with similar examples. It may also be found more systematically by matching the Euler-Lagrangian equation to (2.2.5), equating

coefficients of corresponding terms, and integrating the resulting equations in Lie-algebraic fashion.

The localized regular solitary wave solutions will be found with a Gaussian trial function (2.4.2). Note that it is standard to use such Gaussian ansatzën for analytic tractability. This is true even for simpler nonlinear PDEs where exact solutions may be known and have the usual *sech* or *sech*$^2$ functional forms.

$$\phi = A \exp\left(-\frac{z^2}{\rho^2}\right) \tag{2.4.2}$$

Next, substituting the trial function into the Lagrangian and integrating over all space yields the 'averaged Lagrangian' or action (2.4.3):

$$\frac{A^2\sqrt{\pi}}{72\rho}(-9A^2\rho^2 + 9\sqrt{2}(2+\rho^2) - 8\sqrt{3}A\rho^2 a_2) \tag{2.4.3}$$

The next step is to optimize the trial functions by varying the action with respect to the trial function parameters, viz. the core amplitude, $A$, and the core width, $\rho$. This determines the optimal parameters for the trial function or solitary wave solution, but within the particular functional form chosen for the trial function ansatz. The resulting variational Euler-Lagrange equations, by varying $A$ and $\rho$ respectively, are the system of algebraic equations:

$$\rho^2(3\sqrt{2}a_1 + A(2\sqrt{3}a_2 + 3Aa_3)) = 3\sqrt{2}(1 + \rho^2) \tag{2.4.4}$$

$$\rho^2(18\sqrt{2}a_1 + A(8\sqrt{3}a_2 + 9Aa_3)) = 18\sqrt{2}(-1 + \rho^2) \tag{2.4.5}$$

Given their relative simplicity, and assuming $a_1 = 1/2$, $a_3 = 1$, a nontrivial solution to these equations is

$$A = \frac{4(10 - \rho^2)a_2}{3\sqrt{3}(\rho^2 - 6)} \tag{2.4.6}$$

$$\rho^2 = \frac{80a_2^2 + 2\sqrt{2}(81 - 4\sqrt{81\sqrt{2}a_2^2 + 50a_2^4})}{27\sqrt{2} + 16a_2^2} \tag{2.4.7}$$

The optimized variational soliton for the regular solitary waves of the traveling-wave equation (2.2.5) is given by the trial function (2.4.2) with the above $A$ and $\rho$. The following plots show the resulting regular solitary wave solution for various values of the parameter $a_2$. Note that the tail analysis revealed the need for $a_1 < 1$ in regimes with regular solitary waves.

Figure 2.1 shows the residual of the variational regular solitary waves obtained above. We are able to find this since our variational solution for the regular solitary waves given by (2.4.2), (2.4.6), and (2.4.7) is, unlike for most variational solutions, an analytical one. Inserting this variational solution (2.4.2) (with (2.4.6) and (2.4.7)) into the traveling-wave ODE (2.2.5), the deviation of the left-hand side of (2.2.5) from zero gives a direct measure of the goodness of the variational solution.

Figure 2.2 shows this left-hand side for $a_1 = 1/2$, $a_3 = 1$. For small values of $a_2$, the residual is small for all values of $z$. Greater values of $a_2$ create a greater residual for small values of $z$, but it approaches 0 for any particular $a_2$ as $z \to \infty$.

16
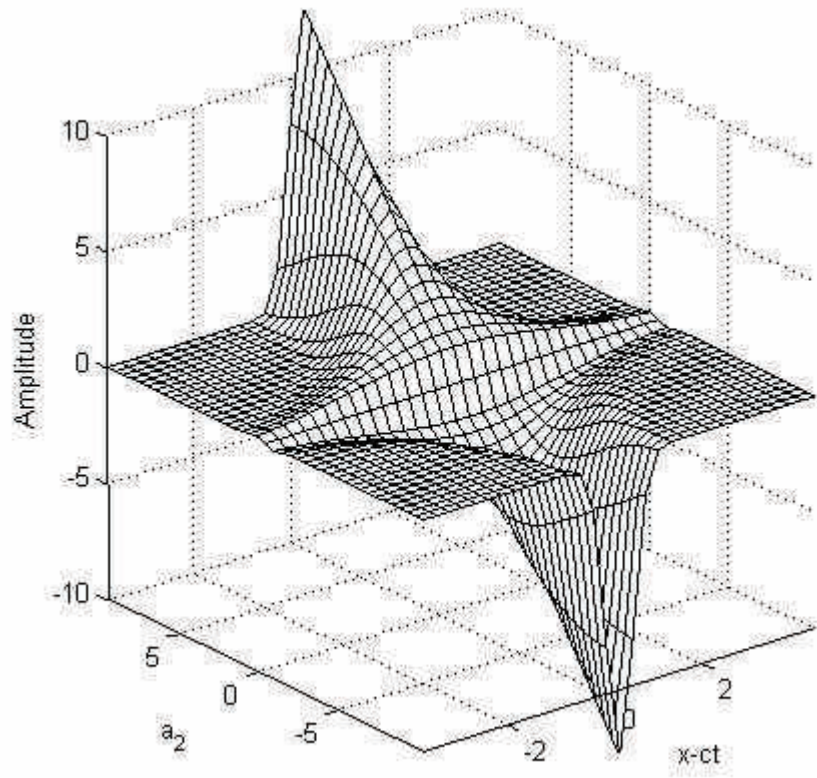
Figure 2.1: The regular soliton plotted for $a_1 = 1/2, a_3 = 1$
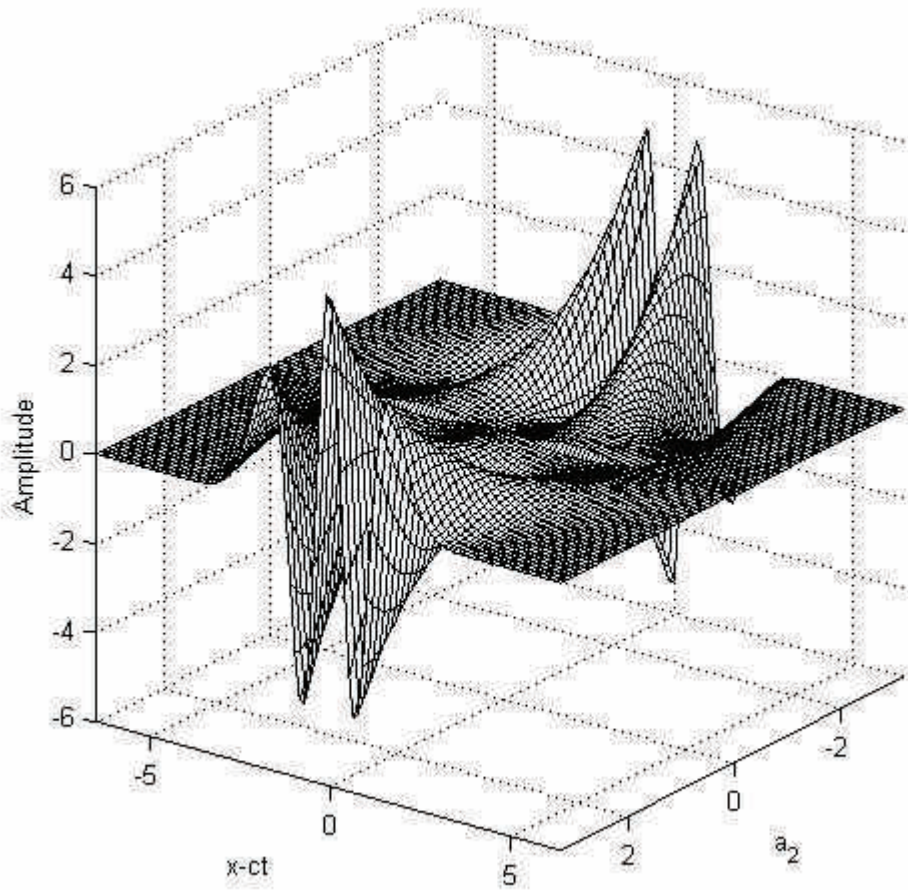
Figure 2.2: Residual of the regular soliton

### 2.4.2 The variational approximation for embedded solitons

In the very recent and novel variational approach to embedded solitary waves, the tail of a delocalized soliton is modeled by (2.4.8). Our embedded solitary wave will be embedded in a sea of such delocalized solitons. The cosine ensures an even solution, and the arbitrary function $\kappa(c)$ will, as shown below, help to ensure the integrability of the action.

$$\phi_{\text{tail}} = \alpha \cos(\kappa(c)z) \qquad (2.4.8)$$

Our ansatz for the embedded soliton uses a second order exponential core model plus the above tail model.

$$\phi = A \exp\left(-\frac{z^2}{\rho^2}\right) + \phi_{\text{tail}} \qquad (2.4.9)$$

Plugging this ansatz into the Lagrangian (2.4.1) and reducing the trigonometric powers to double and triple angles yields an equation with trigonometric functions of the double and triple angles, as well as terms linear in $z$. The former would make spatial integration or averaging of the Lagrangian divergent. However, it is possible to rigorously establish, following a procedure analogous to proofs of Whitham's averaged Lagrangian technique [13], that such terms may be averaged out, so we shall set them to zero *a priori.*

The terms linear in $z$ would also cause the Lagrangian to be non-integrable. Hence, we set $\kappa(c)$ as below to force these linear terms to equal 0.

$$\kappa(c) = \pm \frac{\sqrt{-8 + 8a_1 + 3\alpha^2 a_3}}{2\sqrt{2}} \tag{2.4.10}$$

$$a_i = \alpha_i/c^2 \tag{2.4.11}$$

Note that this step, and the preceding step of averaging out trigonometric functions of the higher angles are novel ones for the variational approximation of embedded solitary waves. They are not part of the traditional Rayleigh-Ritz method used for the construction of regular solitary waves.

Next, the rest of the Lagrangian can be integrated over all space to give the action

$$\frac{-A\sqrt{\pi}}{72\rho} \left( -18\sqrt{2}A(1 + \rho^2) + \rho^2 f(a_1, a_2, a_3) \right) \tag{2.4.12}$$

$$f(a_1, a_2, a_3) = 8\sqrt{3}A^2 a_2 + 36\alpha^2 a_2 + 9A^3 a_3 + 9\sqrt{2}A(2a_1 + 3\alpha^2 a_3) \tag{2.4.13}$$

$$a_i = \alpha_i/c^2 \tag{2.4.14}$$

As for the regular solitary waves, the action is now varied with respect to the core amplitude ($A$), the core width ($\rho$), and the small amplitude ($\alpha$) of the oscillating tail

20

to give the following system of equations (2.4.15), (2.4.16), and (2.4.17):

$$\rho^2 \left( 4\sqrt{3}A^2 a_2 + 6\alpha^2 a_2 + 6A^3 a_3 + 3\sqrt{2}A(2a_1 + 3\alpha^2 a_3) \right) = 6\sqrt{2}A(1 + \rho^2)$$

$$(2.4.15)$$

$$8\sqrt{3}A^2 \rho^2 a_2 + 36\alpha^2 \rho^2 a_2 + 9A^3 \rho^2 a_3 + 9\sqrt{2}A(2 - 2\rho^2 + \rho^2(2a_1 + 3\alpha^2 a_3)) = 0$$

$$(2.4.16)$$

$$4a_2 + 3\sqrt{2}Aa_3 = 0 \tag{2.4.17}$$

For strictly embedded solitary waves, which occur on isolated curves in the parameter space where continua of delocalized solitary waves exist, the amplitude of the tail is strictly zero. Once again, this is an extra feature not encountered in the standard variational procedure. Hence, we set $\alpha = 0$ in the above equations in order to recover such embedded solitary waves, yielding

$$\rho^2 \left( 2\sqrt{3}Aa_2 + 3A^2 a_3 + 3\sqrt{2}a_1 \right) = 3\sqrt{2}(1 + \rho^2) \tag{2.4.18}$$

$$\rho^2 \left( 18\sqrt{2}a_1 + A(8\sqrt{3}a_2 + 9Aa_3) \right) = 18\sqrt{2}(\rho^2 - 1) \tag{2.4.19}$$

$$4a_2 + 3\sqrt{2}Aa_3 = 0 \tag{2.4.20}$$
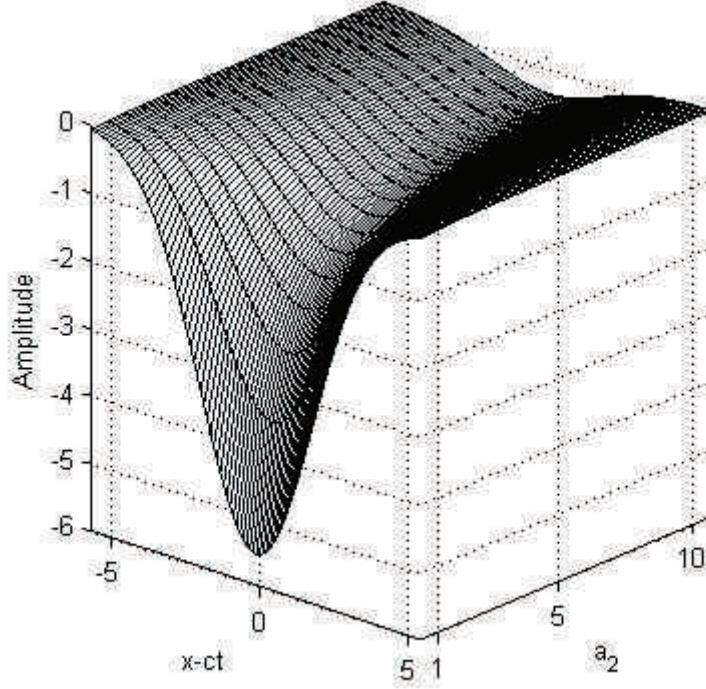
Figure 2.3: The embedded soliton plotted for $a_1 = 2$

If we set $a_1 = 2$, a nontrivial analytical solution to these equations can be found.

$$A = -\frac{2\sqrt{2}a_2}{3a_3} \tag{2.4.21}$$

$$\rho^2 = -\frac{27\sqrt{2}a_3}{12a_2^2 - 8\sqrt{6}a_2^2 + 27\sqrt{2}a_3} \tag{2.4.22}$$

$$a_3 = \frac{-18a_2^2 + 10\sqrt{6}a_2^2}{27\sqrt{2}} \tag{2.4.23}$$

As for the regular solitary waves, our embedded solitary waves (2.4.9) (with $\alpha = 0$ and (2.4.21), (2.4.22), (2.4.23)) are somewhat unusual for the variational approach, being available in analytic form. Hence, as done for the regular solitary waves, they could be inserted into the left-hand of side of (2.2.5), which could then be plotted for various ranges of $z$ and $a_2$. Then, the left-hand side of (2.2.5) again remains very small over all ranges of $z$ and $a_2$, thus attesting to the goodness of the variational embedded solitary waves constructed here.

## 2.5   Conclusion

We have found both regular and embedded solitons in a generalized Pochhammer PDE using a variational method. While both types of solutions are important and relevant in themselves, the approach used for the construction of the embedded solitary waves is novel. It employs several extensions of the conventional Rayleigh-Ritz variational technique, which is a widely used and most versatile technique for the construction of regular solitary waves of important nonlinear PDEs.

# CHAPTER 3
# REGULAR AND EMBEDDED SOLITONS IN A GENERALIZED MICROSTRUCTURE PDE

## 3.1  Abstract

In this chapter, variational methods are employed to generate families of both regular

and embedded solitary wave solutions for a generalized microstructure PDE that is

of great interest. The technique for obtaining the embedded solitons incorporates

several recent generalizations of the usual variational technique and is thus topical in

itself. One unusual feature of the solitary waves derived here is that we are able to

obtain them in analytical form (within the family of the trial functions). Thus, the

residual is calculated, showing the accuracy of the resulting solitary waves. Given the

importance of solitary wave solutions in wave dynamics and information propagation

in nonlinear PDEs, as well as the fact that only the parameter regimes for the

existence of solitary waves had previously been analyzed for the microstructure PDE

considered here, the results obtained here are both new and timely.

## 3.2 Introduction

One-dimensional wave propagation in microstructured solids is currently a topic of great interest, given the potential applications of such materials in diverse areas. This phenomenon has recently been modeled [14] by equation (3.2.1) with complicated dispersive and nonlinear terms.

$$\phi_{tt} - b\phi_{xx} - \frac{\mu}{2}(\phi^2)_{xx} - \delta(\beta\phi_{tt} - \gamma\phi_{xx})_{xx} = 0 \tag{3.2.1}$$

Here, $b$, $\mu$, $\beta$, $\delta$, and $\gamma$ are dimensionless parameters, $\phi$ denoting the macroscopic deformation of the material, and $x$ and $t$ denoting space and time coordinates, respectively.

Equation (3.2.1) is derived by using the so-called Mindlin model in [15–17]. It is a non-integrable PDE. However, necessary analytic conditions for the possible existence of solitary waves of (3.2.1) have been derived in [17, 18]. The last-cited papers also numerically construct asymmetric, pulse-shaped traveling-wave solutions of (3.2.1), where the spatial and temporal coordinates occur in the combination $x-ct$.

More recently [14, 19, 20], pulse trains in (3.2.1) have been numerically patched together.

An analytical method for finding regular and embedded solitons with a variational approach was given in [21]. The method for finding regular solitary waves

variationally is long-standing and widely used. By contrast, that for finding the so-called embedded solitons is of very recent vintage. The embedded solitons are embedded both in the continuous spectrum in spectral space and in a continuum of so-called delocalized solitary waves with oscillatory tails of exponentially small amplitude. In this paper, we shall construct regular solitary waves of (3.2.1) variationally and follow the extensions of that method in [21] to construct embedded soliton families of (3.2.1).

Towards that end and since both types of solitary wave solutions will be traveling-waves, we first derive the traveling-wave reduced ODE corresponding to (3.2.1). First, we transform to the traveling-wave variable $z = x - ct$. The derivatives are transformed as below.

$$\frac{\mathrm{d}}{\mathrm{d}x} = \frac{\mathrm{d}}{\mathrm{d}z}\frac{\mathrm{d}z}{\mathrm{d}x} = \frac{\mathrm{d}}{\mathrm{d}z} \tag{3.2.2}$$

$$\frac{\mathrm{d}}{\mathrm{d}t} = \frac{\mathrm{d}}{\mathrm{d}z}\frac{\mathrm{d}z}{\mathrm{d}t} = c\frac{\mathrm{d}}{\mathrm{d}z} \tag{3.2.3}$$

Now the PDE is an ODE:

$$(c^2 - b)\phi_{zz} - \frac{\mu}{2}(\phi^2)_{zz} - \delta(\beta c^2 \phi_{zz} - \gamma\phi_{zz})_{zz} = 0 \tag{3.2.4}$$

After integrating twice, the PDE becomes the following ODE (3.2.5) governing 1-D longitudinal wave propagation, with parameters defined by (3.2.6) and (3.2.7). Boundary conditions are not taken into account. The solitons constructed for this

equation correspond to homoclinic orbits.

$$\phi_{zz} - q\phi - \frac{1}{2}r\phi^2 = 0 \tag{3.2.5}$$

$$q = \frac{c^2 - b}{\delta(\beta c^2 - \gamma)} \tag{3.2.6}$$

$$r = \frac{\mu}{-\delta(\beta c^2 - \gamma)} \tag{3.2.7}$$

### 3.3   The linear spectrum

As mentioned above, embedded solitary waves exist within a continuum of delocalized solitary waves with oscillating tails, as opposed to the exponentially decaying tails of regular solitary waves. This distinction may be used, together with an analysis of the tail region, to identify the disjoint parameter regimes where each of the two types of solitary waves may exist.

First, we perform a Taylor analysis of the tail of the potential soliton to find parameter regions where regular or embedded solitons could exist. Regular solitary waves have a vanishing amplitude for large $|z|$, and embedded solitary waves will have oscillating tails. These two behaviors can be modeled by an exponential function with either a negative or imaginary argument. We use the simple exponential ansatz

$$\phi = A \exp(\lambda z). \tag{3.3.1}$$

This is plugged into the linearized ODE to find the behavior of the tails. Note that the solution and its derivatives are very small in the tail for both types of solitary wave solutions. This is true even for embedded solitary waves since the tail oscillations have exponentially small amplitudes. Hence, the linearized ODE may be used.

$$\lambda^2 A e^{\lambda z} - q A e^{\lambda z} = 0 \tag{3.3.2}$$

Solving for $\lambda$ reveals the eigenvalues

$$\lambda = \pm\sqrt{q}. \tag{3.3.3}$$

Therefore, parameter regimes with $q > 0$ correspond to regular solitary waves with exponentially decaying tails, while parameter regimes with $q < 0$ support embedded solitons with oscillatory tails.

## 3.4 Variational formulation

### 3.4.1 The variational approximation for regular solitons

The procedure for constructing regular solitary waves with exponentially decaying tails is well-known. It is widely employed in many areas of applied mathematics and goes by the name of the Rayleigh-Ritz method. In this section, we shall employ it to construct regular solitary waves of (3.2.5).

For this purpose, we first require the corresponding Lagrangian. The Lagrangian having equation (3.2.5) as its Euler-Lagrange equation is

$$L = -\frac{q}{2}\phi^2 - \frac{r}{6}\phi^3 + \frac{1}{2}\phi\phi_{zz}. \tag{3.4.1}$$

This may be found by comparison with similar examples. It may also be found more systematically by matching the Euler-Lagrangian equation to (3.2.5), equating coefficients of corresponding terms, and integrating the resulting equations in Lie-algebraic fashion.

The localized regular solitary wave solutions will be found with a Gaussian trial function (3.4.2). Note that it is standard to use such Gaussian ansatzën for analytic tractability. This is true even for simpler nonlinear PDEs where exact solutions may be known and have the usual *sech* or *sech*² functional forms.

$$\phi = A\exp\left(-\frac{z^2}{\rho^2}\right) \tag{3.4.2}$$

Next, substituting the trial function into the Lagrangian and integrating over all space yields the 'averaged Lagrangian' or action (3.4.3):

$$-\frac{A^2}{2}\sqrt{\frac{\pi}{2}}\left(\frac{1}{\rho} + q\rho\right) - \frac{A^3}{6}\sqrt{\frac{\pi}{3}}r\rho \tag{3.4.3}$$

The next step is to optimize the trial function by varying the action with respect to the trial function parameters, viz. the core amplitude, $A$, and the core width, $\rho$. This

determines the optimal parameters for the trial function or solitary wave solution, but within the particular functional form chosen for the trial function ansatz. The resulting variational Euler-Lagrange equations, by varying $A$ and $\rho$ respectively, are the system of algebraic equations:

$$\sqrt{3}Ar\rho^2 + 3\sqrt{2}(1 + qp^2) = 0 \qquad (3.4.4)$$

$$2\sqrt{3}Ar\rho^2 + 9\sqrt{2}(-1 + q\rho^2) = 0 \qquad (3.4.5)$$

Given their relative simplicity, a nontrivial solution to these equations is

$$A = -\frac{6\sqrt{6}q}{5r} \qquad (3.4.6)$$

$$\rho^2 = \frac{5}{q} \qquad (3.4.7)$$

The optimized variational soliton for the regular solitary waves of the traveling-wave equation (3.2.5) is given by the trial function (3.4.2) with the above $A$ and $\rho$. Figures 3.1 and 3.2 show the resulting regular solitary wave solution for $q = 1$ and various values of the parameter $r$, as well as for $r = 1$ and various positive values of $q$. Note that the tail analysis revealed the need for positive $q$ in regimes with regular solitary waves.

Figures 3.3 and 3.4 show a direct analysis of the accuracy of the variational regular solitary waves obtained above. In this instance, we are able to calculate the residual since our variational solution for the regular solitary waves given by (3.4.2), (3.4.6),
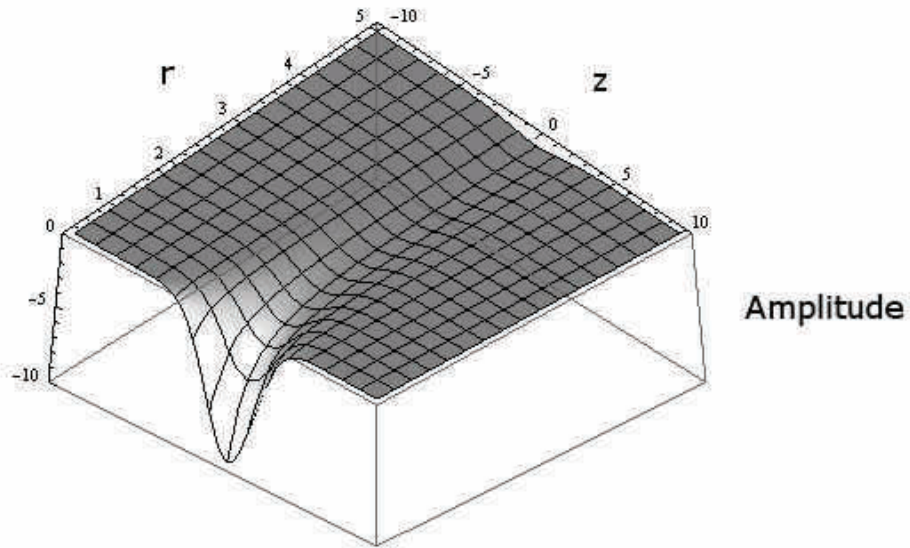
Figure 3.1: The regular soliton plotted for $q = 1$
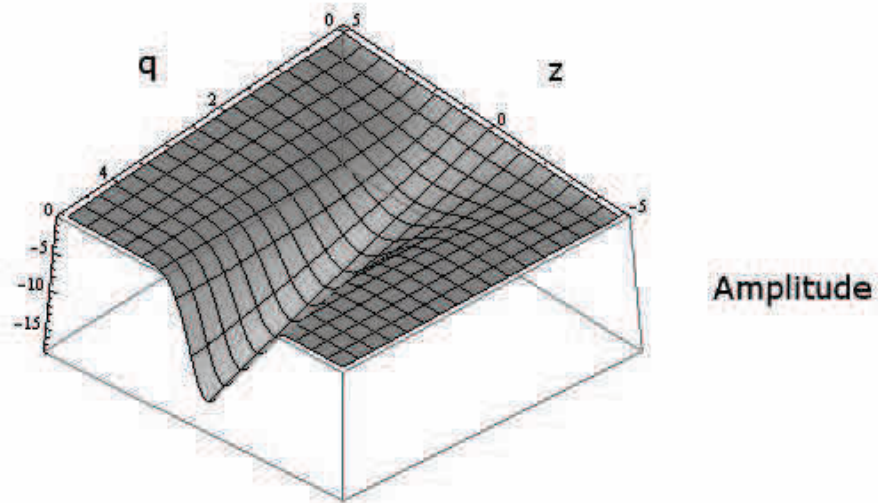


Figure 3.2: The regular soliton plotted for $r = 1$
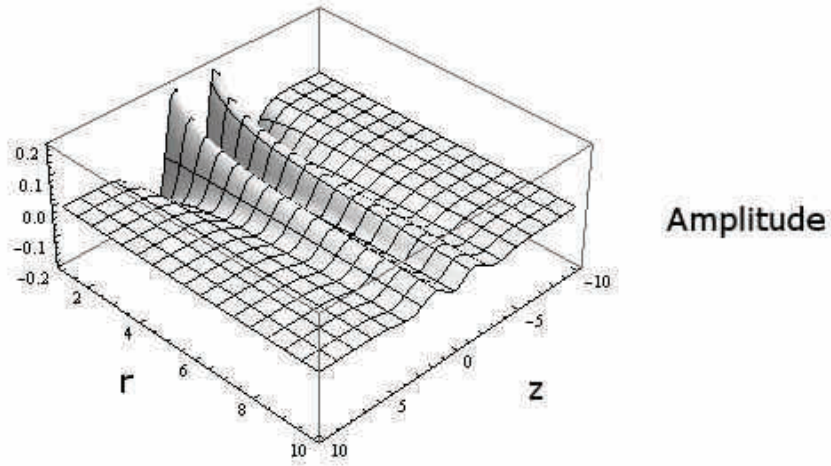
Figure 3.3: Residual of the regular soliton for $q = 1$

and (3.4.7) is, unlike for most variational solutions, an analytical one. Inserting this variational solution (3.4.2) (with (3.4.6) and (3.4.7)) into the traveling-wave ODE (3.2.5), the deviation of the left-hand side of (3.2.5) from zero gives a direct measure of the goodness of the variational solution.

Figure 3.3 shows this left-hand side for $q = 1$. Over the entire ranges of $z$ from -10 to 10 and $r$ from 1 to 10, it is bounded in magnitude by 0.2, thus showing that our variational solution is indeed accurate over the entire range of $z$ and $r$ values. At larger $z$ values, the residual becomes even smaller. At values of $r$ less than 1
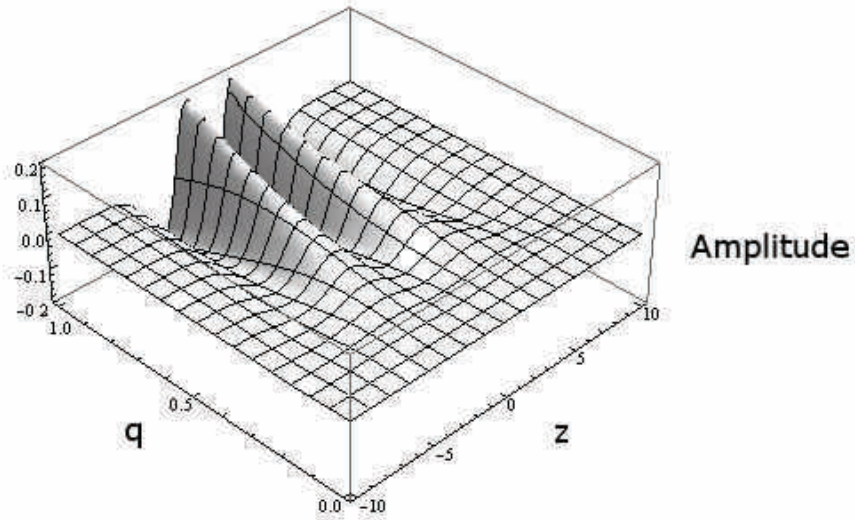
Figure 3.4: Residual of the regular soliton for $r = 1$

and approaching 0, the residual increases without bound since there is an $r$ in the denominator of (3.4.6).

Figure 3.4 displays the left-hand side of (3.2.5) in a somewhat different fashion. Now, $r = 1$. Over the entire ranges of $z$ from -10 to 10 and $q$ from 0 to 1, it is bounded in magnitude by 0.2, thus showing that our variational solution is, once again, accurate over the entire range of $z$ and small $q$ values. At larger $z$ values, the deviation from zero becomes even smaller. The residual increases for larger values of $q$.

33

### 3.4.2 The variational approximation for embedded solitons

In the very recent and novel variational approach to embedded solitary waves, the tail of a delocalized soliton is modeled by (3.4.8). Our embedded solitary wave will be embedded in a sea of such delocalized solitons. The cosine ensures an even solution, and the arbitrary function $\kappa(c)$ will, as shown below, help to ensure the integrability of the action.

$$\phi_{\text{tail}} = a\cos(\kappa(c)z) \tag{3.4.8}$$

Our ansatz for the embedded soliton uses a fourth order exponential core model plus the above tail model.

$$\phi = A\exp\left(-\frac{z^4}{\rho^4}\right) + \phi_{\text{tail}} \tag{3.4.9}$$

Plugging this ansatz into the Lagrangian (3.4.1) and reducing the trigonometric powers to double and triple angles yields an equation with trigonometric functions of the double and triple angles, as well as terms linear in $z$. The former would make spatial integration or averaging of the Lagrangian divergent. However, it is possible to rigorously establish, following a procedure analogous to proofs of Whitham's averaged Lagrangian technique [13], that such terms may be averaged out, so we shall set them to zero *a priori*.

The terms linear in $z$ would also cause the Lagrangian to be non-integrable. Hence, we set $\kappa(c) = \pm\sqrt{\alpha}$, where $\alpha = -q > 0$, to force these linear terms to equal zero. Note that this step, and the preceding step of averaging out trigonometric functions of the higher angles are novel ones for the variational approximation of embedded solitary waves. They are not part of the traditional Rayleigh-Ritz method used for the construction of regular solitary waves.

Next, the rest of the equation can be integrated to give the action

$$-\frac{1}{18}A\left(9a^2r + A(2\cdot 3^{3/4}Ar - 9\cdot 2^{3/4}\alpha)\right)\rho\Gamma\left[\frac{5}{4}\right] - \frac{1}{\rho}2^{1/4}A^2\Gamma\left[\frac{7}{4}\right] \qquad (3.4.10)$$

Here we have used the Gamma function $\Gamma$. As for the regular solitary waves, the action is now varied with respect to the core amplitude ($A$), the core width ($\rho$), and the small amplitude ($a$) of the oscillating tail to give the following system of equations (3.4.11), (3.4.12), and (3.4.13):

$$\left(3a^2r + 2A(3^{3/4}Ar - 3\cdot 2^{3/4}\alpha)\right)\rho^2\Gamma\left[\frac{5}{4}\right] + 12\cdot 2^{1/4}A\Gamma\left[\frac{7}{4}\right] = 0 \qquad (3.4.11)$$

$$\left(9a^2r + A(2\cdot 3^{3/4}Ar - 9\cdot 2^{3/4}\alpha)\right)\rho^2\Gamma\left[\frac{5}{4}\right] - 18\cdot 2^{1/4}A\Gamma\left[\frac{7}{4}\right] = 0 \qquad (3.4.12)$$

$$aAr\rho = 0 \qquad (3.4.13)$$

For strictly embedded solitary waves, which occur on isolated curves in the parameter space where continua of delocalized solitary waves exist, the amplitude of the tail is strictly zero. Once again, this is an extra feature not encountered in the standard

35
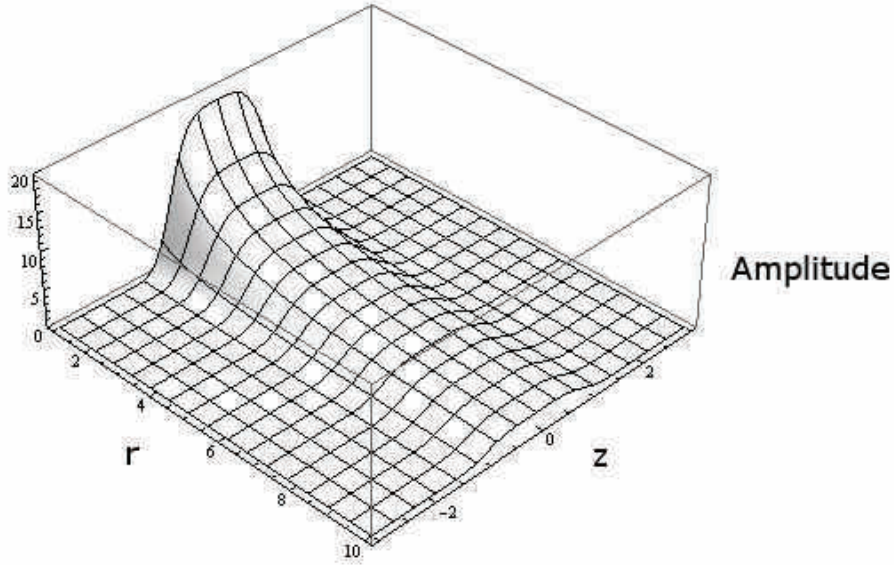
Figure 3.5: The embedded soliton plotted for $\alpha = 7$

variational procedure. Hence, we set $a = 0$ in the above equations in order to recover

such embedded solitary waves, yielding

$$(3^{3/4}Ar - 3 \cdot 2^{3/4}\alpha)\rho^2 \Gamma\left[\frac{5}{4}\right] + 6 \cdot 2^{1/4}\Gamma\left[\frac{7}{4}\right] = 0 \qquad (3.4.14)$$

$$(2 \cdot 3^{3/4}Ar - 9 \cdot 2^{3/4}\alpha)\rho^2 \Gamma\left[\frac{5}{4}\right] - 18 \cdot 2^{1/4}\Gamma\left[\frac{7}{4}\right] = 0 \qquad (3.4.15)$$

A nontrivial analytical solution to these equations is found to be

$$A = \frac{2^{7/4}3^{5/4}\alpha}{5r} \qquad (3.4.16)$$

$$\rho^2 = -2^{1/2}\frac{5}{\alpha}\frac{\Gamma[7/4]}{\Gamma[5/4]} \qquad (3.4.17)$$
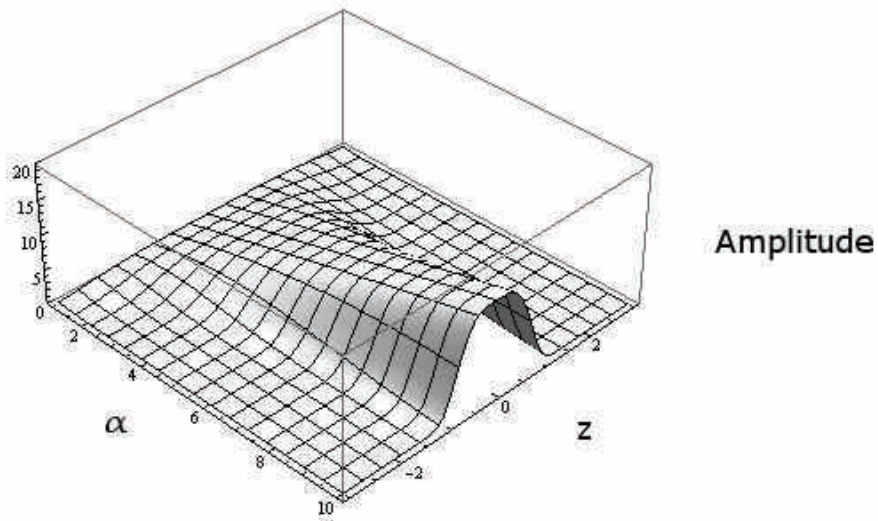
Figure 3.6: The embedded soliton plotted for $r = 2$

Note that using the model $\exp(-z^2/\rho^2)$ for the core of the embedded solitary wave, with the tail (3.4.8) added on, would have resulted in an imaginary $\rho$, which would have made the argument to the exponential positive, and there would have been no decaying wave corresponding to a genuine embedded solitary wave. Figures 3.5 and 3.6 show our embedded soliton (3.4.9) (with $a = 0$ and (3.4.16)/(3.4.17)) versus the traveling-wave variable $z$ for figure 3.5: $\alpha = 7$ and various $r$ values and figure 3.6: $r = 2$ and various positive values of $\alpha$. Note that the tail analysis revealed the need for negative $q$ values (positive $\alpha$ values) in order to have delocalized solitary waves with oscillatory tails.
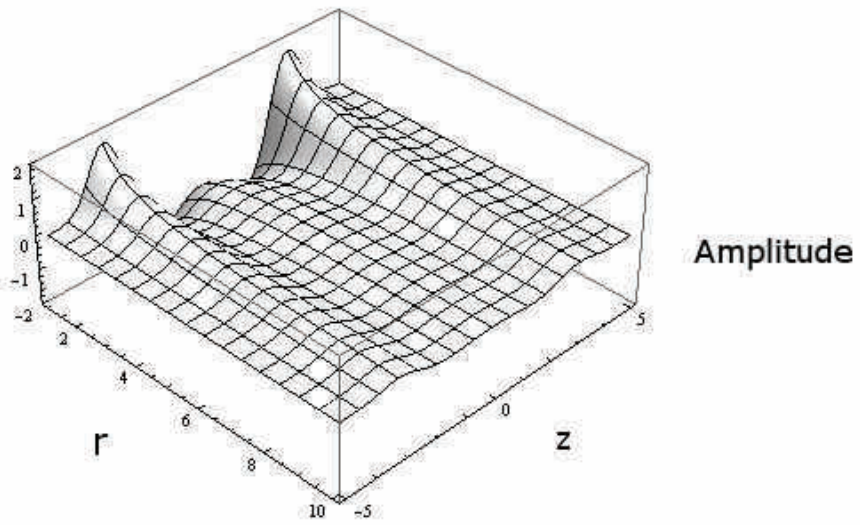
Figure 3.7: Residual of the embedded soliton for $\alpha = 1$
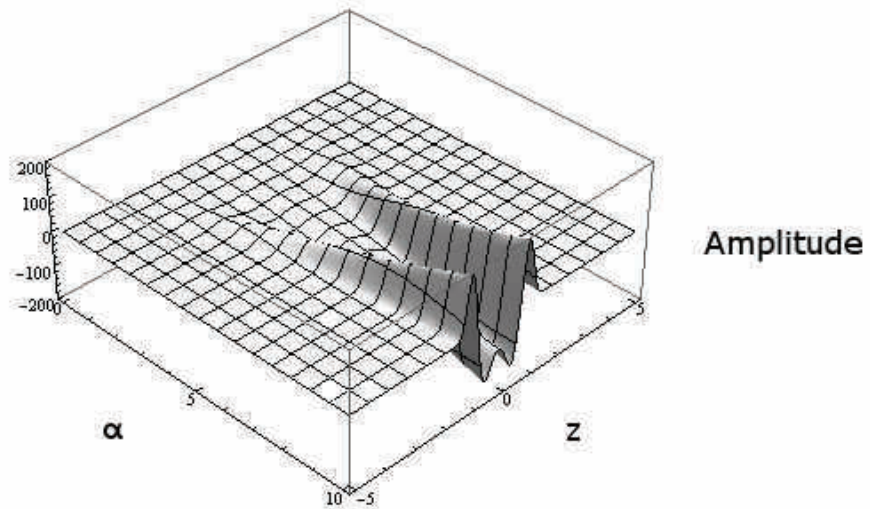


Figure 3.8: Residual of the embedded soliton for $r = 1$

As for the regular solitary waves, our embedded solitary waves (3.4.9) (with $a = 0$ and (3.4.16)/(3.4.17)) are somewhat unusual for the variational approach, being available in analytic form. Hence, as done for the regular solitary waves, figures 3.7 and 3.8 show (3.4.9) inserted into the left-hand of side of (3.2.5), which is then plotted for various ranges of $z$, $r$ and $\alpha$. The residual again remains very small for fixed $\alpha$ and large enough $r$ and $z$, and for fixed $r$ and large enough $z$ or small enough $\alpha$, thus attesting to the goodness of the variational embedded solitary waves constructed here.

## 3.5   Conclusion

We have found both regular and embedded solitons in a topical, generalized microstucture PDE using a variational method. While both types of solutions are important and relevant in themselves, the approach used for the construction of the embedded solitary waves is novel. It employs several extensions of the conventional Rayleigh-Ritz variational technique, which is a widely used and most versatile technique for the construction of regular solitary waves of important nonlinear PDEs.

**Part III**

# DYNAMICAL CONSEQUENCES FOR GENERALIZED HOPF BIFURCATIONS

# CHAPTER 4
# GENERALIZED HOPF BIFURCATIONS AND QUASIPERIODICITY IN A LASER DIODE SYSTEM WITH SELF-SUSTAINED PULSATIONS

## 4.1 Abstract

In this chapter, generalized Hopf bifurcations in a laser diode system are considered. The periodic orbit immediately following the generalized Hopf bifurcation is constructed using the method of multiple scales, and its stability is analyzed. Numerical solutions reveal the existence of stable periodic attractors, attractors at infinity, and bounded chaotic dynamics in various cases. The dynamics are explained on the basis of the bifurcations occurring. Chaotic regimes are characterized using power spectra, auto-correlation functions and fractal dimensions.

## 4.2 Introduction

In this chapter, we consider a semiconductor laser diode system [22, 23] with self-sustained pulsation (SSN). In normalized coordinates [23], the equations governing this system are written below, where $\tau$ is normalized time, $x$ and $y$ are normalized

41

carrier densities in different sections of the diode, $z$ is a normalized photon number density, $\bar{\tau}_b$ is a normalized carrier lifetime, $\gamma$ is the ratio of the differential gains in the two sections, $\bar{\Gamma}$ is a photon loss coefficient, and $x_0$ and $y_0$ are normalized photon pumping rates in the two sections.

$$\dot{x}(\tau) = -(x - x_0) - xz,$$
$$\dot{y}(\tau) = -\frac{(y - y_0)}{\bar{\tau}_b} - \gamma yz, \qquad (4.2.1)$$
$$\dot{z}(\tau) = \bar{\Gamma}(x + y - 1)z,$$

Physically, the parameters that may be varied most readily are the pumping rates $x_0$ and $y_0$. The other parameters, $\bar{\tau}$, $\gamma$ and $\bar{\Gamma}$, are material properties of the semiconductor and thus difficult to vary.

Hopf and generalized Hopf bifurcations occur in this system. The conditions for their occurrence are analyzed, and the resulting periodic orbits are constructed analytically by the method of multiple scales. Stability analysis of these periodic orbits reveals that they may be destroyed by secondary bifurcations as the parameter is varied further past the bifurcation value. These secondary bifurcations may lead to chaos. This conclusion is verified numerically, showing that while the periodic orbit serves as a vehicle for SSN, which keeps the system operating in a microwave oscillator mode, it does so over a narrow range of parameters.

The remainder of this chapter is organized as follows. In section 4.3 we consider the stability of the fixed point of (4.2.1) and the onset of instability via a Hopf bifurcation, which may be either supercritical or subcritical. In section 4.4, we derive the analytical expressions for the periodic orbits resulting from this generalized Hopf bifurcation by employing the method of multiple scales. Section 4.5 considers detailed numerical solutions and discusses the results.

## 4.3 Linear stability and generalized Hopf bifurcation analysis

The fixed (alternatively, equilibrium or critical) points of (4.2.1) are $(x_c, y_c, z_c)$, defined in (4.3.1).

$$
\begin{aligned}
x_c &= \frac{-1 + \gamma\bar{\tau}_b + \gamma\bar{\tau}_b x_0 + y_0 \pm \sqrt{D}}{2(\gamma\bar{\tau}_b - 1)} \\
y_c &= \frac{-1 + \gamma\bar{\tau}_b - \gamma\bar{\tau}_b x_0 - y_0 \mp \sqrt{D}}{2(\gamma\bar{\tau}_b - 1)} \\
z_c &= \frac{-1 - \gamma\bar{\tau}_b + \gamma\bar{\tau}_b x_0 + y_0 \mp \sqrt{D}}{2\gamma\bar{\tau}_b} \\
D &= (1 + \gamma\bar{\tau}_b - \gamma\bar{\tau}_b x_0 - y_0)^2 + 4\gamma\bar{\tau}_b(x_0 + y_0 - 1)
\end{aligned}
\tag{4.3.1}
$$

Here we pick the fixed point satisfying the physical requirement $z_c > 0$ [22, 23]. Following standard methods of phase-plane analysis [22], the Jacobian matrix of

43

(4.2.1) at $(x_c, y_c, z_c)$ is

$$J = \begin{pmatrix} -\frac{x_0}{x_c} & 0 & -x_c \\ 0 & -\frac{1}{\bar{\tau}_b} - \gamma\left(\frac{x_0}{x_c} - 1\right) & -\gamma(1 - x_c) \\ \bar{\Gamma}\left(\frac{x_0}{x_c} - 1\right) & \bar{\Gamma}\left(\frac{x_0}{x_c} - 1\right) & 0 \end{pmatrix}$$

The eigenvalues of this matrix satisfy the characteristic equation (4.3.2);

$$\lambda^3 + b_1\lambda^2 + b_2\lambda + b_3 = 0 \qquad (4.3.2)$$

$$b_1 = \frac{1}{\bar{\tau}_b} - \gamma + \frac{(1 + \gamma)x_0}{x_c}$$

$$b_2 = x_c(-1 + \gamma)\bar{\Gamma} + \frac{x_0}{x_c}\left(\frac{1}{\bar{\tau}_b} + \gamma(-1 + \bar{\Gamma})\right) + \left(\frac{x_0}{x_c}\right)^2 \gamma$$

$$- \bar{\Gamma}(\gamma + (-1 + \gamma)x_0) \qquad (4.3.3)$$

$$b_3 = -\bar{\Gamma}(x_c - x_0)\left(\frac{1}{\bar{\tau}_b} - \gamma + x_c^{-2}\gamma x_0\right)$$

For $(x_c, y_x, z_c)$ to be a stable fixed point within the linearized analysis, all the eigenvalues must have negative real parts [22]. From the Routh-Hurwitz criterion, the necessary and sufficient conditions for the solutions of (4.3.2) to have negative real parts are

$$b_1 > 0, \quad b_3 > 0, \quad b_1b_2 - b_3 > 0. \qquad (4.3.4)$$

The condition $b_1b_2 - b_3 = 0$ for Hopf bifurcation yields an involved equation. In order to solve this, the simplest technique is to isolate the $\sqrt{D}$ terms on one side and then

square to obtain an expression which is of sixth degree in $x_0$ and $y_0$ (and contains spurious solutions due to squaring). Since the resulting equation is not transparent, we do not include it here. If the two relevant values of $x_0$ satisfying $b_1 b_2 - b_3 = 0$ are $x_{01}$ and $x_{02}$, then the following is true: (a) If $x_{01} > 0$, then $(x_c, y_c, z_c)$ is stable for $0 < x_0 < x_{01}$ and $x_0 > x_{02}$ and unstable for $x_{01} < x_0 < x_{02}$; (b) If $x_{01} < 0$, then $(x_c, y_c, z_c)$ is stable for $x_0 > x_{02}$ and unstable for $0 < x_0 < x_{02}$.

In this chapter, we will primarily be concerned with the interesting case of the generalized Hopf bifurcation scenario where all three roots of (4.3.2) have zero real parts, which corresponds to the first two Routh-Hurwitz conditions becoming marginal, i.e.,

$$b_1 = b_3 = 0 \tag{4.3.5}$$

Sets of system parameters satisfying these conditions for the generalized Hopf bifurcation will be considered in section 4.5.

In the next section, we construct the orbits arising through the generalized Hopf bifurcation and consider their stability.

## 4.4 Analytical construction of orbits

We will use the method of multiple scales to construct analytical approximations for the orbits arising through the generalized Hopf bifurcation of the fixed point of the laser-diode system. For the system of differential equations (4.2.1), the only physically relevant fixed point is given by (4.3.1). The parameter $x_0$ will be used as the control parameter. The limit cycle is determined by expanding about the fixed point using progressively slower time scales. The expansion takes the following form.

$$x = x_c + \sum_{n=1}^{2} \epsilon^n x_n(T_0, T_1, T_2) + \cdots , \tag{4.4.1}$$

$$y = y_c + \sum_{n=1}^{2} \epsilon^n y_n(T_0, T_1, T_2) + \cdots , \tag{4.4.2}$$

$$z = z_c + \sum_{n=1}^{2} \epsilon^n z_n(T_0, T_1, T_2) + \cdots , \tag{4.4.3}$$

Here $T_n = \epsilon^n \tau$ and $\epsilon$ is a small positive non-dimensional parameter that is introduced as a bookkeeping device and will be set to unity in the final analysis. Utilizing the chain rule, the time derivative becomes

$$\frac{d}{d\tau} = D_0 + \epsilon D_1 + \epsilon^2 D_2 + \cdots , \tag{4.4.4}$$

$$D_n = \partial/\partial T_n$$

The delay parameter $x_0$ is ordered as follows.

$$x_0 = x_{0c} + \epsilon \mu_1 + \epsilon^2 \mu_2, \tag{4.4.5}$$

Here $x_{0c}$ is obtained from (4.3.5). This is standard for this method, as it allows the influence from the nonlinear terms and the control parameter to occur at the same order.

Using (4.4.1)-(4.4.5) in (4.2.1) and equating like powers of $\epsilon$ yields equations at $O(\epsilon^i)$, $i = 1, 2$ of the following form.

$$L_1(x_i, y_i, z_i) = S_{i,1}, \tag{4.4.6}$$

$$L_2(x_i, y_i, z_i) = S_{i,2}, \tag{4.4.7}$$

$$L_3(x_i, y_i, z_i) = S_{i,3}, \tag{4.4.8}$$

Here, $L_i$, $i = 1, 2$ are the differential operators below.

$$L_1(x_i, y_i, z_i) \equiv D_0 x_i + x_i + x_c z_i + z_c x_i \tag{4.4.9}$$

$$L_2(x_i, y_i, z_i) \equiv D_0 y_i + \frac{y_i}{\bar{\tau}_b} + \gamma y_c z_i + \gamma z_c y_i \tag{4.4.10}$$

$$L_3(x_i, y_i, z_i) \equiv D_0 z_i + \bar{\Gamma}(z_i - x_c z_i - y_c z_i - z_c x_i - z_c y_i). \tag{4.4.11}$$

The source terms $S_{i,j}$ for $i = 1, 2$ and $j = 1, 2, 3$, i.e. at $O(\epsilon)$ and $O(\epsilon^2)$ are

$$S_{1,1} = \mu_1$$

$$S_{1,2} = 0$$

$$S_{1,3} = 0$$

$$S_{2,1} = -D_1 x_1 - x_1 z_1 + \mu_2 \tag{4.4.12}$$

$$S_{2,2} = -D_1 y_1 - \gamma y_1 z_1$$

$$S_{2,3} = -D_1 z_1 + \bar{\Gamma} x_1 z_1 + \bar{\Gamma} y_1 z_1$$

Note that (4.4.8) may be solved for $y_i$ in terms of $z_i$ and $x_i$. Using this in (4.4.7) yields $z_i$ in terms of $x_i$. Next, using both of these last two relations in (4.4.6) yields the composite equation below.

$$L_c x_i = \Gamma_i, \tag{4.4.13}$$

The composite operator $L_c$ is defined below.

$$L_c \equiv \frac{L_{cn3} D_0^3 + L_{cn2} D_0^2 + L_{cn1} D_0 + L_{cn0}}{x_c z_c \bar{\Gamma} \bar{\tau}_b} \tag{4.4.14}$$

$$L_{cn3} = \bar{\tau}_b$$

$$L_{cn2} = 1 + \bar{\tau}_b + z_c \bar{\tau}_b + z_c \gamma \bar{\tau}_b$$

$$L_{cn1} = 1 + z_c + z_c(x_c \bar{\Gamma} + \gamma(1 + z_c - x_c \bar{\Gamma})) \bar{\tau}_b$$

$$L_{cn0} = z_c \bar{\Gamma}(x_c + (y_c + z_c) \gamma \bar{\tau}_b)$$

The composite source term $\Gamma_i$ is defined below.

$$\Gamma_i \equiv \left( \gamma \left( 1 - \frac{1}{x_c} \right) + \frac{D_0^2}{x_c z_c \bar{\bar{\Gamma}}} + \frac{D_0(1 + \bar{\tau}_b z_c \gamma)}{\bar{\tau}_b x_c z_c \bar{\bar{\Gamma}}} \right) S_{i,1}$$

$$- S_{i,2} - \left( \frac{D_0}{z_c \bar{\bar{\Gamma}}} - \frac{1 + \bar{\tau}_b z_c \gamma}{z_c \bar{\bar{\Gamma}} \bar{\tau}_b} \right) S_{i,3}. \tag{4.4.15}$$

We shall use (4.4.13) and (4.4.14) later to identify and suppress secular terms in the solutions of (4.4.6)-(4.4.8).

Let us now turn to finding the solutions of (4.4.6)-(4.4.8). For $i = 1$ or $O(\epsilon)$, we may pick the following form for the first order carrier density below.

$$x_1 = \alpha(T_1)e^{\lambda_1 \tau} + \beta(T_1)e^{\lambda_2 \tau} + \eta(T_1)e^{\lambda_3 \tau}, \tag{4.4.16}$$

Here $\beta = \bar{\alpha}$ is the complex conjugate of $\alpha$ since $\lambda_2 = \bar{\lambda}_1$ and $x_1$ is a real carrier density. The $\alpha$, $\beta$ and $\eta$ correspond to the center manifold where the $\lambda_{1,2}$ are purely imaginary and $\lambda_3 = 0$.

Using (4.4.16) in (4.4.6)-(4.4.8) for $i = 1$ together with (4.4.12) yields the first order fields

$$y_1 = -\frac{(x_c z_c \bar{\Gamma} + \lambda_1(1 + z_c + \lambda_1))}{x_c z_c \bar{\Gamma}} \alpha(T_1)e^{\lambda_1 \tau}$$

$$- \frac{(x_c z_c \bar{\Gamma} + \lambda_2(1 + z_c + \lambda_2))}{x_c z_c \bar{\Gamma}} \beta(T_1)e^{\lambda_2 \tau} - \eta(T_1), \tag{4.4.17}$$

$$z_1 = -\frac{(1 + z_c + \lambda_1)}{x_c} \alpha(T_1)e^{\lambda_1 \tau} - \frac{(1 + z_c + \lambda_2)}{x_c} \beta(T_1)e^{\lambda_2 \tau}$$

$$- \frac{(1 + z_c)}{x_c} \eta(T_1) + \frac{\mu_1}{x_c} \tag{4.4.18}$$

49

Now that the first order solutions (4.4.16)-(4.4.18) are known, the second order sources $S_{2,1}$ through $S_{2,3}$ may be evaluated via (4.4.12). Setting the coefficients of the secular $e^{\lambda_{1,2,3}t}$ terms in these sources (which are the solutions of the homogeneous equations for $i = 1$) to zero yields the normal form:

$$D_1\alpha = \alpha(k_1\mu_1 + k_2\eta), \tag{4.4.19}$$

$$D_1\eta = k_3\mu_2 + k_4\alpha\beta + k_5\mu_1\eta + k_6\eta^2, \tag{4.4.20}$$

where we have used $\lambda_1 = i\omega$ and $\lambda_2 = -i\omega$, and

$$k_1 = -k_{1N}/k_{1D} \tag{4.4.21}$$

$$k_{1N} = z_c^2 \gamma \bar{\Gamma} \bar{\tau}_b + i \left( -1 + z_c^2 \gamma \bar{\tau}_b \right) \omega + (1 + \bar{\tau}_b)\omega^2 + i\bar{\tau}_b \omega^3$$

$$k_{1D} = x_c z_c (-1 - 2i(1 + \bar{\tau}_b)\omega + 3\bar{\tau}_b \omega^2$$

$$+ (-1 - \gamma\bar{\tau}_b(1 + \bar{\Gamma} + 2i\omega) - 2i\bar{\tau}_b\omega - (1 - \gamma)\bar{\Gamma}\bar{\tau}_b x_c)z_c - \gamma\bar{\tau}_b z_c^2)$$

$$k_2 = k_{2N}/k_{2D} \tag{4.4.22}$$

$$k_{2N} = 2z_c^2(1 + z_c)\gamma\bar{\Gamma}\bar{\tau}_b + i \left( -1 + z_c^2 + z_c^2\gamma(2 + 2z_c + \bar{\Gamma})\bar{\tau}_b \right) \omega$$

$$+ \left( 1 - \left( -1 + z_c^2(1 + \gamma) \right) \bar{\tau}_b \right) \omega^2 + i\bar{\tau}_b\omega^3$$

$$k_{2D} = x_c z_c (1 + 2i(1 + \bar{\tau}_b)\omega - 3\bar{\tau}_b\omega^2 + (1 + \gamma\bar{\tau}_b(1 + \bar{\Gamma} + 2i\omega)$$

$$+ 2i\bar{\tau}_b\omega + (1 - \gamma)\bar{\Gamma}\bar{\tau}_b x_c)z_c + \gamma\bar{\tau}_b z_c^2)$$

$$k_3 = \frac{\gamma\bar{\Gamma}\bar{\tau}_b y_c z_c}{1 + (1 + \gamma(1 + \bar{\Gamma})\bar{\tau}_b + (1 - \gamma)\bar{\Gamma}\bar{\tau}_b x_c)z_c + \gamma\bar{\tau}_b z_c^2} \tag{4.4.23}$$

$$k_4 = \frac{2z_c(1 + z_c)\gamma\bar{\Gamma}\bar{\tau}_b}{x_c(1 + z_c + z_c(x_c\bar{\Gamma} + \gamma(1 + z_c + y_c\bar{\Gamma}))\bar{\tau}_b)} \tag{4.4.24}$$

$$k_5 = -\frac{z_c\gamma\bar{\Gamma}\bar{\tau}_b}{x_c(1 + z_c + z_c(x_c\bar{\Gamma} + \gamma(1 + z_c + y_c\bar{\Gamma}))\bar{\tau}_b)} \tag{4.4.25}$$

$$k_6 = \frac{z_c(1 + z_c)\gamma\bar{\Gamma}\bar{\tau}_b}{x_c(1 + z_c + z_c(x_c\bar{\Gamma} + \gamma(1 + z_c + y_c\bar{\Gamma}))\bar{\tau}_b)}. \tag{4.4.26}$$

Writing $\alpha = ae^{i\theta}$, the real and imaginary parts of (4.4.19) yield

$$\frac{\partial a}{\partial T_1} = k_{1,r}\mu_1 a + k_{2,r}\eta a, \tag{4.4.27}$$

51

and

$$a \frac{\partial \theta}{\partial T_1} = k_{1,i} \mu_1 a + k_{2,i} \eta a, \tag{4.4.28}$$

where

$$k_{1,2} = k_{1,2\,r} + i k_{1,2\,i}. \tag{4.4.29}$$

The fixed points of (4.4.20) and (4.4.27) are

$$\eta = \eta_c = -\frac{k_{1,r}}{k_{2,r}} \mu_1 \tag{4.4.30}$$

$$a = a_c = \sqrt{\frac{k_3 \mu_2 - \frac{k_{1,r} k_5 \mu_1^2}{k_2} + \frac{k_{1,r}^2 k_6 \mu_1^2}{k_2^2}}{-k_4}} \tag{4.4.31}$$

Using these values in the first order field yields the post-generalized Hopf periodic orbits.

$$x_1 = (a_c e^{i\theta} e^{i\omega\tau} + a_c e^{-i\theta} e^{-i\omega\tau}) + \eta_c$$

$$= 2 a_c \cos(\omega\tau + \theta) + \eta_c \tag{4.4.32}$$

The evolution and stability of the periodic orbit (4.4.32) of amplitude $a_c$ is governed by the stability of the fixed point $a_c$ of (4.4.27) and (4.4.28). To determine this, we compute the Jacobian (and eigenvalue, as this is a one-dimensional system)

of (4.4.27) at $a = a_c$, $\eta = \eta_c$, i.e.,

$$
\begin{aligned}
J &= \frac{\partial}{\partial a} \left( k_{1,r} \mu_1 a + k_{2,r} \eta a \right) \Big|_{(a_c, \eta_c)} \\
&= k_{1,r} \mu_1 + k_{2,r} \eta_c \\
&\equiv 0 \qquad \text{by (4.4.30)}.
\end{aligned}
$$

Since this eigenvalue is non-hyperbolic, or has zero real part, our linearized stability analysis of the periodic orbits (4.4.32) is inconclusive. Hence, we shall determine this via direct numerical simulations on (4.2.1) in the post-generalized Hopf regime.

To this end, we consider actual parameter sets for the occurrence of the generalized Hopf bifurcation and the subsequent dynamics in the next section.

## 4.5   Numerical results

As is well known, the supercritical Hopf bifurcations give rise to a stable or attracting periodic orbit. By contrast, the subcritical Hopf bifurcation corresponds to an unstable periodic orbit coexisting with a stable fixed point. This unstable periodic orbit tightens like a noose around the fixed point as the perturbed parameter approaches the bifurcation value. At the bifurcation value, the two collide, causing the fixed point to become unstable. Thus, there is neither a stable fixed point attractor nor

53

a stable limit cycle attractor. Hence, one may have one of three possible dynamical behaviors:

(a) bounded quasiperiodic dynamics,

(b) bounded chaotic dynamics, or

(c) solutions may go to an attractor at infinity (a movable, initial condition dependent singularity [24]) in a finite time.

However, in this chapter we are interested in degenerate Hopf bifurcations which do not satisfy the "simple eigenvalue hypothesis," and so we should not expect the standard Hopf bifurcation diagrams to describe the behavior we see on either side of the bifurcation point.

In the case of a regular Hopf bifurcation in three dimensions, one pair of eigenvalues of the Jacobian matrix evaluated at the fixed point are complex conjugates with zero real parts, and the other eigenvalue is free. This free eigenvalue is also the trace of the matrix since the other two sum to zero, and so its value determines the dissipativity of the system. A large negative trace would be helpful for finding interesting chaotic behavior. In the case of a generalized Hopf bifurcation in three dimensions, the third eigenvalue is zero, and so the trace is also zero.
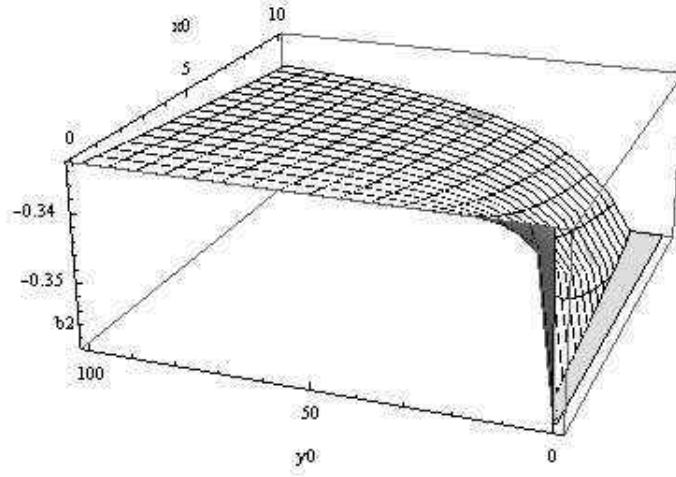
Figure 4.1: The characteristic polynomial coefficient $b2$ for small positive parameter values should always be positive for physically meaningful parameter sets. Shown here for small positive parameter values, the surface is always negative.

And so, we now move on to numerical solutions. Physically realistic parameter values would be positive and on the order of 1. Figure 4.1 shows the coefficient of the characteristic polynomial $b2$, which should always be positive since it is equal to the square of the frequency of the periodic orbit. In the figure, made with small positive parameter values, $b2$ is always negative. Figure 4.2 show the coefficients $b1$ and $b3$, which should equal zero simultaneously. Again, with small parameters on the order of 1, the figure indicates that this is not possible.

To proceed, we need values for the fixed point as well as for the bifurcation point of the control parameter. For the purpose of this analysis we will consider two cases
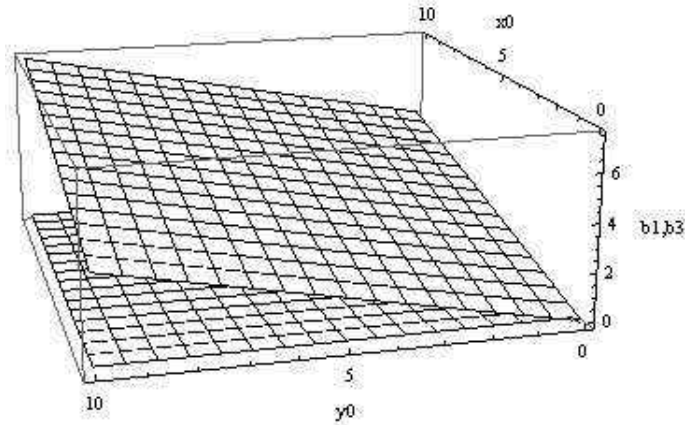
Figure 4.2: The characteristic polynomial coefficients $b1$ and $b3$ for small positive parameter values should vanish simultaneously at the bifurcation. Shown here for small positive parameter values, the surfaces do not intersect at 0.

corresponding to the following sets of numerical values:

$$x0 = 0.98730, \quad \gamma = 53, \quad \theta = 143, \quad \tau b = -0.75748 \tag{4.5.1}$$

$$y0 = 0.00019457, \quad \gamma = 95, \quad \theta = 80, \quad \tau b = -0.0083491, \tag{4.5.2}$$

These parameter sets give positive values for the fixed points.

For (4.5.1), the fixed point is given by

$$(x_c, y_c, z_c) \approx (0.98148, 0.018519, 0.0059290) \tag{4.5.3}$$

and the bifurcation occurs at

$$y0 \approx 0.014111. \tag{4.5.4}$$

Furthermore, the eigenvalues of the Jacobian at the fixed point with these parameters are

$$\lambda_{1,2} = \pm 0.80770i, \quad \lambda_3 = 0. \tag{4.5.5}$$

The corresponding values for (4.5.2) are

$$(x_c, y_c, z_c) \approx (0.98958, 0.010417, 1.2372) \tag{4.5.6}$$

$$x0 \approx 2.2139 \tag{4.5.7}$$

$$\lambda_{1,2} = \pm 13.816, \lambda_3 = 0. \tag{4.5.8}$$

For parameter set (4.5.1), we begin integrating at $(x_c + ic\delta, y_c + ic\delta, z_c + ic\delta)$ where $ic\delta = 10^{-6}$. Figure 4.3 shows quasiperiodic behavior in the time series of $x(t)$ on one side of the bifurcation, $y0 - 10^{-6}$. Figure 4.4 shows that $y(t)$ approaches infinity on the other side, $y0 + 10^{-6}$. Figure 4.5 shows the behavior of the trajectories near the quasiperiodic attractor in the $(x, y, z)$ phase-space.

For the parameter set (4.5.2), we also begin integrating at $(x_c + ic\delta, y_c + ic\delta, z_c + ic\delta)$ where $ic\delta = 10^{-6}$. On one side of the bifurcation, $x0 - 10^{-6}$, Figure 4.6 reveals strange aperiodic behavior in $y(t)$.

To analyze this motion, we show the power spectral density in figure 4.7 and the autocorrelation function in Figure 4.8. Both have been computed using code from "Numerical Recipes in C" [25]. The broad features in the power spectral density

show that power is being injected into many different frequencies, which is indicative of chaos. The autocorrelation function first goes to zero at $t_c = 2$. This is used as the time delay in the fractal dimension calculation [24–35] which is discussed below.

A more quantitative and definitive numerical diagnostic is the fractal dimension. Strong randomness or stochastic behavior with many degrees of freedom can be distinguished from low-dimensional (deterministic) chaos by computing the fractal cluster dimension. Of several possible alternative definitions for the fractal dimension [24–35] we employ the cluster fractal dimension $D$ of Termonia and Alexandrowicz [29] which is defined below.

$$n = k[R(n)]^D, \quad n \to \infty \tag{4.5.9}$$

Here $R(n)$ is the average radius of an $E$-dimensional ball containing $n$ points. Thus, $D$ is the slope of a plot of $\log n$ versus $\log R(n)$. More usefully, if a scaling law (4.5.9) exists, then it would show up on a plot of $d \log n / d \log R(n)$ versus $\log n$, with the height of the line being a measure of $D$. Numerical computation of $D$ is somewhat subtle, and requires the embedding of the numerical time-series $N(t)$ in $E$-dimensional space with various values of $E$, via the construction (from $N(t)$) of

"$E$-tuples"

$$[N(t), N(t + \tau), N(t + 2\tau), \ldots, N(t + (E - 1)\tau)], \qquad (4.5.10)$$

$$[N(t + \tau), N(t + 2\tau), \ldots, N(t + E\tau)], \ldots \qquad (4.5.11)$$

This is a consequence of the Takens embedding theorem [24–35]. For each choice of embedding dimension $E$, the "delay" $\tau$ is typically chosen to be $t_c$, $t_c/2$ and $2t_c$ and $D$ is estimated for each $\tau$ from the slope of a $\log n / \log R(n)$ plot (provided this is approximately a straight line, or there is a well-defined scaling region) or the height of an approximate horizontal line in a $(\mathrm{d} \log n / \mathrm{d} \log R(n)) / \log n$ plot. This is repeated for increasing $E$ until the estimates for $D$ saturate, which yields the converged estimate for $D$ (provided well-defined straight lines or scaling regions (4.5.9) occur in the plots and the $D$ values obtained for $\tau = t_c, t_c/2$, and $2t_c$ are in good agreement). Following this procedure, a sample plot is shown in Figure 4.9.

Figure (4.9) shows the $(\mathrm{d} \log n / \mathrm{d} \log R(n)) / \log n$ plot for $E = 3$, $t_c = \tau$. From the height of the approximate horizontal line (which indicates a well-defined scaling region), we can estimate the converged cluster fractal dimension to be a non-integer value in the range $D \in (1.27, 1.32)$. This confirms that the system possesses bounded low-dimensional (deterministic) chaotic solutions evolving on a strange attractor with fractal dimension $D \in (1.27, 1.32)$.
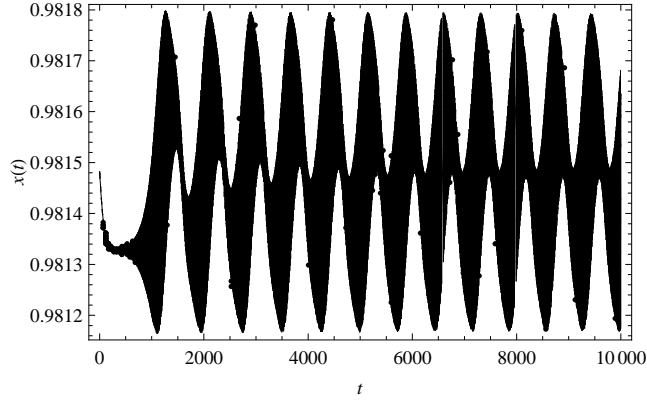
Figure 4.3: A quasiperiodic time series for $x(t)$ for parameter set 4.5.1 and the perturbation $y0 - 10^{-6}$.

In conclusion, we have comprehensively analyzed generalized Hopf bifurcations in our laser-diode model. In contrast to regular Hopf bifurcations [36], which give rise to a very stable and robust periodic attractor in this system, the generalized Hopf bifurcation creates stable quasiperiodic attractors and chaotic attractors. These attractors are, once again, very robust under subsequent parameter changes in the post-bifurcation regime. Thus, as for the stable periodic attractors resulting from regular Hopf bifurcation, these generalized-Hopf induced solutions provide a robust, and very desirable, platform for quasiperiodic operation of the laser-diode systems over a large region of the parameter space.
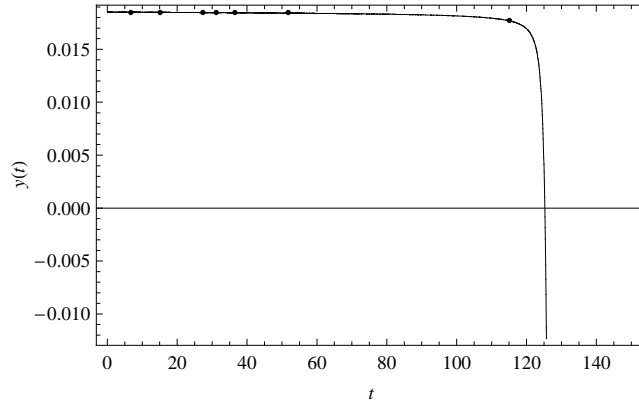
Figure 4.4: The variable $y(t)$ approaches infinity for parameter set 4.5.1 and the perturbation $y0 + 10^{-6}$.
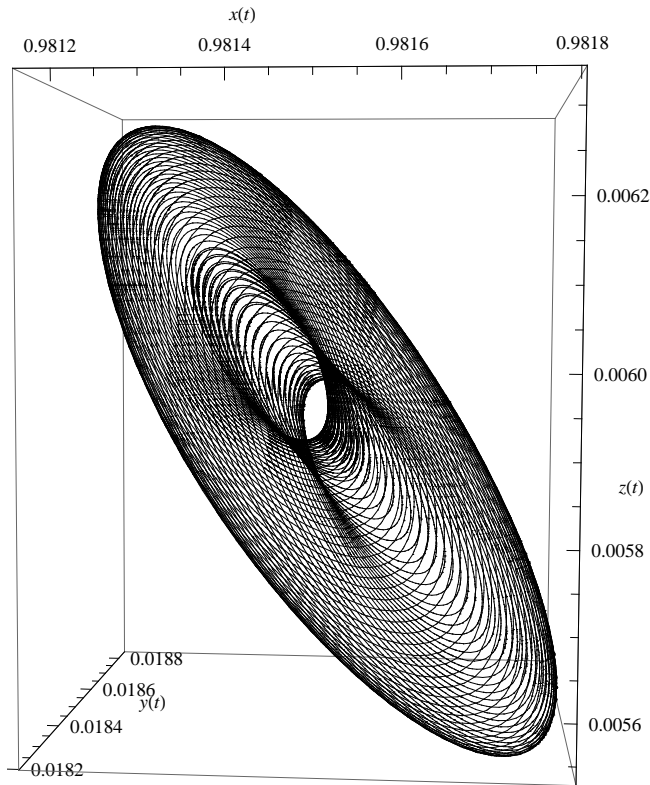


Figure 4.5: A quasiperiodic orbit in the $(x, y, z)$ phase space for parameter set 4.5.1 with perturbation $y0 - 10^{-6}$.
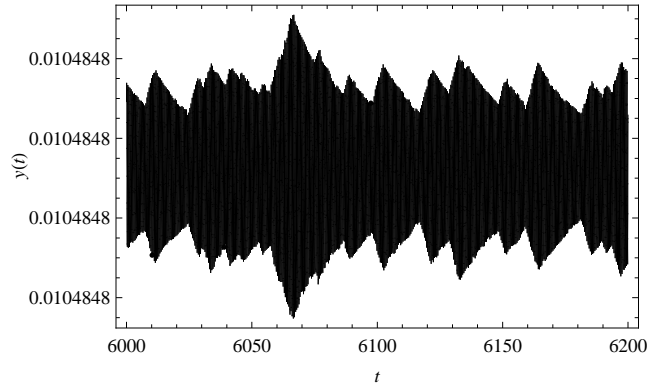
Figure 4.6: Chaotic behavior in the time series of $y(t)$ for parameter set 4.5.2 with perturbation $x0 - 10^{-6}$.
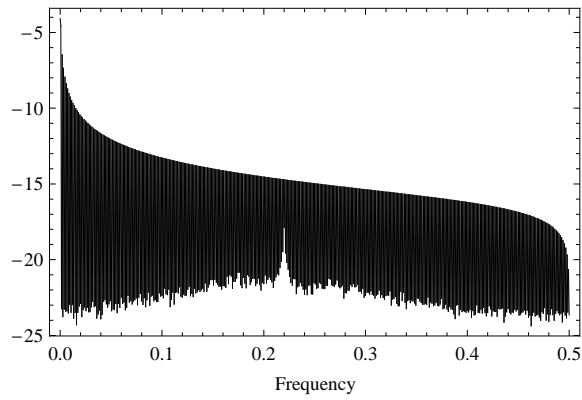


Figure 4.7: Power spectrum for $y(t)$ with perturbation $x0 - 10^{-6}$. Broad features show lots of contributing frequencies which indicates chaos.
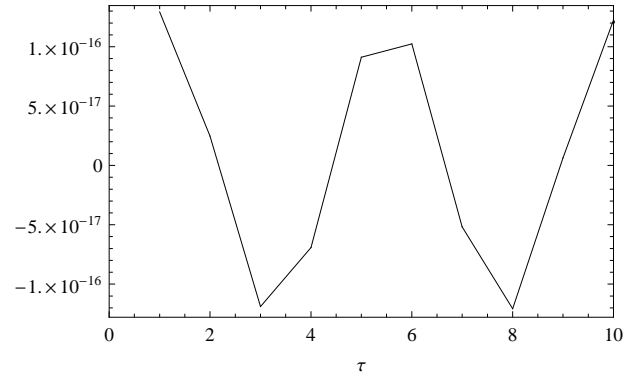
Figure 4.8: Autocorrelation for $y(t)$ with perturbation $x0 - 10^{-6}$. The value goes to zero at $t_c = 2$.
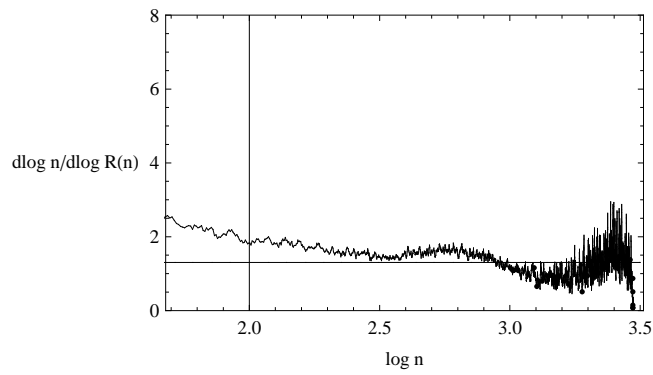


Figure 4.9: Fractal cluster dimension for $y(t)$ with perturbation $x0 - 10^{-6}$ is $D \in (1.27, 1.32)$.

# CHAPTER 5
# GENERALIZED HOPF BIFURCATIONS AND CHAOS
# IN A PREDATOR-PREY SYSTEM

## 5.1    Abstract

In this chapter, generalized Hopf bifurcations in a predator-prey model with delay terms modeled by "weak generic kernel $a \exp(-at)$" are considered. The periodic orbit immediately following the generalized Hopf bifurcation is constructed using the method of multiple scales, and its stability is analyzed. Numerical solutions reveal the existence of attractors at infinity and bounded chaotic dynamics in various cases. The dynamics are explained on the basis of the bifurcations occurring in each. Chaotic regimes are characterized using power spectra, correlation functions, and fractal dimensions.

## 5.2    Introduction

Population models for single-species, two-species, and multispecies communities are of relevance in various fields of mathematical biology and mathematical ecology. Extensive reviews of various continuous models have been investigated (such as the

64

regular logistic equation for one species, Lotka-Volterra systems for two species and a variety of additional effects as in the Kolmogorov, May, Holling, Hsu, Leslie, Caperon and other models) and may be found, for example, in [37, 38]. Discrete models are considered there.

In order to incorporate various realistic physical effects that may cause at least one of the physical variables to depend on the past history of the system, time-delays often need to be introduced into the governing equations. Factors that introduce time lags may include age structure of the population (influencing the birth and death rates), maturation periods (thresholds), feeding times and hunger coefficients in predator-prey interactions, reaction times, food storage times, and resource re-generation times. Models incorporating time delays in diverse biological models are extensively reviewed by MacDonald [39] and, in the context of predator-prey models, by Cushing [37].

Consider, for instance, the (modified) Lotka-Volterra two-species model below.

$$\dot{N}(t) = \epsilon N(1 - N/\kappa) - \alpha NP,$$

$$\dot{P}(t) = \gamma P + \beta NP \tag{5.2.1}$$

Here $N(t)$ and $P(t)$ are the prey and predator populations (numbers) respectively, $\epsilon$ is the birth rate of the prey, $\kappa > 0$ is the carrying capacity, $\alpha$ is the rate of predation per predator, $\gamma$ is the death rate of the predator, $\beta$ is the rate of the prey's

contribution to the predator growth, and the overdot denotes a time derivative. Farkas [40] has considered the modification of (5.2.1) when a distributed (Volterra or convolution-type [41]) delay was introduced in the second equation, yielding the following equations.

$$\dot{N}(t) = \epsilon N(1 - N/\kappa) - \alpha N P \tag{5.2.2}$$

$$\dot{P}(t) = -\gamma P + \beta P \int_{-\infty}^{t} N(\tau)\bar{G}(t - \tau)d\tau \tag{5.2.3}$$

Here $\bar{G}(U)$ is the memory function of delay kernel [39, 41]. Similarly, El-Owaidy and Ammar [42] have considered (5.2.1) modified to include delays in both equations, i.e.,

$$\dot{N}(t) = \epsilon N - \alpha N P - \frac{\epsilon N}{\kappa} \int_{-\infty}^{t} N(\tau)\bar{G}(t - \tau)d\tau \tag{5.2.4}$$

$$\dot{P}(t) = -\gamma P + \beta P \int_{-\infty}^{t} N(\tau)\bar{G}(t - \tau)d\tau. \tag{5.2.5}$$

One choice for the memory function is the Dirac delta function, which is sometimes referred to as the unit impulse function. The defining properties of this function are

$$\delta(t - a) = 0, \quad t \neq a,$$

$$\int_{-\infty}^{\infty} \delta(t - a)d\tau = 1. \tag{5.2.6}$$

For $\bar{G}(U) = \delta(U)$, one gets the case of the so-called discrete delay [37–39, 41]. While both (5.2.3) and (5.2.5) may be treated in the setting of the theory of functional

66

differential equations [21, 37, 39, 43], employing the "linear chain" form has proven fruitful for the memory function [39, 44, 45]. Reference [39] discusses the origin of this in the theory of elasticity and in the work of Vogel [21, 43].

$$\bar{G}(U) = G_a^p(U) \equiv \frac{a^{p+1}U^p}{p!}e^{-aU} \tag{5.2.7}$$

Notice that in this model, $1/a$ measures the influence of the past, and as $a$ increases, this influence decreases. The functions $G_1^0(U)$ and $G_a^1(U)$ (which are called the 'weak' and 'strong' kernels [37]) have been used in [44, 45] in the context of predator-prey models, such as May's model [37].

In [40, 42], the authors used the memory function $G_a^{(0)}(U)$ to investigate the systems (5.2.3) and (5.2.5), respectively. This reduces the integrodifferential systems (5.2.3) and (5.2.5) to the differential systems:

$$\dot{N}(t) = \epsilon N(1 - N/\kappa) - \alpha NP, \tag{5.2.8}$$

$$\dot{P}(t) = \gamma P_\beta PQ \tag{5.2.9}$$

$$\dot{Q}(t) = a(N - Q)$$

$$\dot{N}(t) = \epsilon N(1 - Q/\kappa) - \alpha NP, \tag{5.2.10}$$

$$\dot{P}(t) = -\gamma P + \beta PQ$$

$$\dot{Q}(t) = a(N - Q),$$

Here the definition of $\dot{Q}(t)$ is given below.

$$\dot{Q}(t) \equiv \int_{-\infty}^{t} N(\tau)\bar{G}(t-\tau)d\tau$$

$$= \int_{-\infty}^{t} N(\tau)ae^{-a(t-\tau)}d\tau \tag{5.2.11}$$

In particular, Farkas [40] showed that at $a = a_0 \equiv \beta\kappa - \gamma - \epsilon/\beta\kappa$ a supercritical Hopf bifurcation [46] takes place for the system (5.2.8), and the bifurcating closed paths are asymptotically stable for $a < a_0$. A companion theorem was also derived, which provides simpler sufficient, but not necessary, conditions for the stability of the bifurcating closed periodic orbits. El-Owaidy and Ammar [42] showed analogously that for (5.2.10), a supercritical Hopf bifurcation takes place at $a = a_0 \equiv \beta\kappa - \gamma > 0$ (if $\beta\kappa - \gamma > 0$), and the bifurcating closed periodic orbits are orbitally asymptotically stable for $a < a_0$.

In this chapter, we will extend the analyses of references [40, 42] to the general predator-prey model with distributed delay in both prey and predator equations:

$$\dot{N}(t) = NF(N) - \alpha NP - \frac{\tilde{\epsilon}N}{\kappa}\int_{-\infty}^{t} N(\tau)\bar{G}(t-\tau)d\tau,$$

$$\dot{P}(t) = -PG(P) + \beta P \int_{-\infty}^{t} N(\tau)\bar{G}(t-\tau)d\tau. \tag{5.2.12}$$

For $F(N) = \epsilon = $ constant, $G(P) = \gamma = $ constant, and $\tilde{\epsilon} = \epsilon$, this model would reduce to (5.2.5). For $\tilde{\epsilon} = 0$, $F(N) = \epsilon(1 - N/\kappa)$ and $G(P) = \gamma = $ constant, the model (5.2.12) reduces to (5.2.3). Notice that qualitative features of such general

models have been considered earlier, for instance for the Kolmogorov model without delay [38] and the May model with delay [37] using $G_a^0(U)$ and $G_a^1(U)$. Here, however, we will follow references [40, 42, 46, 47], using $G_a^0(U)$ to consider the stability of the fixed points (equilibria) and the Hopf bifurcations of (5.2.12) for the general functions $F(N)$ and $G(P)$. This is done in Section 5.3. An analogous treatment of these issues for the special case of (5.2.12) with $\tilde{\epsilon} = 0$ has been considered by Roose [48]. In Section 5.4 we consider (5.2.12) for specific choices of $F(N)$ and $G(P)$ to determine the regions of phase-space where the system is dissipative (volume contracting) or dilatory (volume expanding). Section 5.5 considers the stability of physically relevant equilibria and Hopf bifurcation points for specific parameter values and choices of $F(N)$ and $G(P)$. Possible chaotic regimes are also delineated there. The systems are numerically integrated, and chaotic regimes are characterized by computing power spectra, correlation functions and fractal dimensions [49].

In the remainder of this chapter, we shall consider generalized Hopf bifurcations in (5.2.12) with $\bar{G}(U) = G_a^0(U)$, which yields the differential system below.

$$\dot{N}(t) = NF(N) - \alpha NP - \frac{\tilde{\epsilon}QN}{\kappa} \tag{5.2.13}$$

$$\dot{P}(t) = -PG(P) + \beta PQ$$

$$\dot{Q}(t) = a(N - Q),$$

Here $Q$ defined by (5.2.11). This system has been investigated earlier [49] for functions $F$ and $G$ different from those considered here, although the primary emphasis there was on characterizing chaotic regimes using numerical diagnostics. Here, we shall carefully consider the solutions resulting from generalized Hopf bifurcations. We shall derive analytic expressions for the resulting periodic orbits using the method of multiple scales. The stability of this periodic orbit is then considered, revealing secondary bifurcation of the orbit leading to chaos. Also, note that $F(N)$ is chosen to incorporate the prey birth rate. Later we will consider, as a typical example, the function below.

$$F(N) = 1 - \delta N \tag{5.2.14}$$

Similarly, the function $G(P)$ incorporates the predator death rate and is chosen so that this rate increases with predator density $P$. A typical example, and the one we will use, is

$$G(P) = \gamma(1 + \kappa P^2). \tag{5.2.15}$$

The remainder of this chapter is organized as follows. In Section 5.3, we consider the stability of the fixed point of (5.2.13)-(5.2.15) and the onset of instability via Hopf and generalized Hopf bifurcations that may be either supercritical or subcritical. In Section 5.4, we derive analytical expressions for the periodic orbits resulting from

generalized Hopf bifurcations by employing the method of multiple scales. Section 5.5

considers detailed numerical solutions and discusses the results.

### 5.3 Linear stability and generalized Hopf bifurcation analysis

The fixed (also known as equilibrium or critical) points of (5.2.13) (remembering

that only points with positive $N$ and $P$ are physically applicable) are $(N_0, P_0, Q_0)$.

$$N_0 = Q_0 = \frac{\alpha^2 \beta \kappa + 2\tilde{\epsilon}\gamma\kappa + 2\delta\gamma\kappa^2 - \alpha D}{2\gamma(\tilde{\epsilon} + \delta\kappa)^2} \tag{5.3.1}$$

$$P_0 = \frac{-\alpha\beta\kappa + D}{2\gamma\kappa(\tilde{\epsilon} + \delta\kappa)} \tag{5.3.2}$$

$$D^2 \equiv \alpha^2\beta^2\kappa^2 - 4\gamma\kappa(\tilde{\epsilon} + \delta\kappa)(\tilde{\epsilon}\gamma - \beta\kappa + \delta\gamma\kappa) \tag{5.3.3}$$

Here we pick the fixed point $(N_0, P_0, Q_0)$ corresponding to positive values of the prey

and predator populations $N_0$ and $P_0$, and omit the four fixed points with vanishing

values for either or both of these populations. Following standard methods of phase-

plane analysis, the Jacobian matrix of (5.2.13) at $(N_0, P_0, Q_0)$ is

$$J = \begin{pmatrix} N_0 F'(N_0) & -\alpha N_0 & -\frac{\tilde{\epsilon} N_0}{\kappa} \\ 0 & -P_0 G'(P_0) & \beta P_0 \\ a & 0 & -a \end{pmatrix} \tag{5.3.4}$$

The eigenvalues of this matrix satisfy the characteristic equation and coefficients given below.

$$\lambda^3 + b_1\lambda^2 + b_2\lambda + b_3 = 0 \tag{5.3.5}$$

$$b_1 = L + a$$

$$b_2 = aL - N_0 P_0 F'G' + \tilde{\epsilon}aN_0/\kappa \tag{5.3.6}$$

$$b_3 = aN_0 P_0(\alpha\beta - F'G' + \tilde{\epsilon}G'/\kappa)$$

$$L = 2\kappa\gamma P_0^2 + \delta N_0$$

$$F' = -\delta \tag{5.3.7}$$

$$G' = 2\kappa\gamma P_0$$

For $(N_0, P_0, Q_0)$ to be a stable fixed point within the linearized analysis, all the eigenvalues must have negative real parts. The necessary and sufficient conditions for (5.3.5) to have $Re(\lambda_{1,2,3}) < 0$ flow from the Routh-Hurwitz criterion:

$$b_1 > 0, \quad b_3 > 0, \quad b_1 b_2 - b_3 > 0.$$

Using (5.3.7), $b_1 > 0$ is satisfied since both $a$ and $\kappa$ are positive. The next condition is also satisfied when the fixed point $(N_0, P_0, Q_0)$ has $F' < 0$, i.e., if $\delta > 0$ (recalling that $G'(P)$ is everywhere positive). The final condition is satisfied when

$$f(a) \equiv a^2 \left( L + \frac{\tilde{\epsilon}N_0}{\kappa} \right) + a \left( L^2 + \frac{\tilde{\epsilon}N_0 L}{\kappa} - \alpha\beta N_0 P_0 - \frac{\tilde{\epsilon}G'N_0 P_0}{\kappa} \right) - LN_0 P_0 F'G' > 0.$$

This is satisfied when there are no real roots of $f(a) = 0$. The existence of at least one real positive root of $f(a) = 0$ at $a_0$ corresponds to a change of stability of the fixed point $(N_0, P_0, Q_0)$, since (5.3.8) is violated.

$$a_0 = \frac{\Gamma \pm \sqrt{\Gamma^2 + 4LN_0P_0F'G'(N_0\epsilon + L\kappa)}}{2(L\kappa + N_0\epsilon)} \tag{5.3.9}$$

$$\Gamma = -LN_0\epsilon + G'N_0P_0\epsilon - L^2\kappa + N_0P_0\alpha\beta\kappa \tag{5.3.10}$$

Note that in previous research, the inequality corresponding to (5.3.8) governing the change in stability is only linear in $a$. If the discriminant is negative in (5.3.9), then $a_0$ is complex, and the fixed point $(N_0, P_0, Q_0)$ is stable for all the physically relevant values of $a$ (since (5.3.8) is satisfied for $a = 0$ with $F' < 0$). If the discriminant is positive, on the other hand, and we call the two real solutions for $a_0$ in (5.3.8) $a_{01}$ and $a_{02}$, then there are two possible scenarios. If $a_{01} > 0$, then $(N_0, P_0, Q_0)$ is stable for $0 < a < a_{01}$ and $a > a_{02}$ and unstable for $a_{01} < a < a_{02}$, or else, if $a_{01} < 0$, then the fixed point is stable for $a > a_{02}$, and unstable for $0 < a < a_{02}$.

In this chapter, we will primarily be concerned with the interesting case of the generalized Hopf bifurcation scenario in which all roots of (5.3.5) have zero real parts, which corresponds to the first two Routh-Hurwitz conditions becoming marginal, i.e.,

$$b_1 = b_3 = 0 \tag{5.3.11}$$

Sets of system parameters satisfying these conditions for the generalized Hopf bifurcation will be considered in Section 5.5.

In the next section, we construct the orbits arising through the generalized Hopf bifurcation and consider their stability.

## 5.4 Analytical construction of periodic orbits

We will use the method of multiple scales to construct analytical approximations for the periodic orbits arising through the generalized Hopf bifurcations of the fixed point of the predator-prey model. For the system of differential equations (5.2.12), with $F(N)$ and $G(P)$ given by (5.2.14) and (5.2.15), respectively, the only physically relevant fixed point is given by (5.3.2).

The parameter $a$ will be used as the control parameter. The limit cycle is determined by expanding around the fixed point using progressively slower time scales.

The expansion takes the form below.

$$N = N_0 + \sum_{n=1}^{3} \epsilon^n N_n(T_0, T_1, T_2) + \ldots \tag{5.4.1}$$

$$P = P_0 + \sum_{n=1}^{3} \epsilon^n P_n(T_0, T_1, T_2) + \ldots \tag{5.4.2}$$

$$Q = Q_0 + \sum_{n=1}^{3} \epsilon^n Q_n(T_0, T_1, T_2) + \ldots, \tag{5.4.3}$$

Here $T_n = \epsilon^n t$ and $\epsilon$ is a small non-dimensional parameter that is introduced as a bookkeeping device and will be set to unity in the final analysis. Utilizing the chain rule, the time derivative is expanded as shown below.

$$\frac{d}{dt} = D_0 + \epsilon D_1 + \epsilon^2 D_2 + \ldots, \tag{5.4.4}$$

Here $D_n = \partial/\partial T_n$. The delay parameter $a$ is ordered as below where $a_0$ is derived from the condition that $b_1 = b_3 = 0$.

$$a = a_0 + \epsilon a_1 + \epsilon^2 a_2 \tag{5.4.5}$$

Using (5.4.1)-(5.4.5) and equating like powers of $\epsilon$ yields equations at $O(\epsilon^i)$, $i = 1, 2, 3$ of the form:

$$L_1(N_i, P_i, Q_i) = S_{i,1} \tag{5.4.6}$$

$$L_2(N_i, P_i, Q_i) = S_{i,2} \tag{5.4.7}$$

$$L_3(N_i, P_i, Q_i) = S_{i,3} \tag{5.4.8}$$

Here the $L_i$, $i = 1, 2, 3$ are the following differential operators

$$L_1(N_i, P_i, Q_i) \equiv D_0 N_i + \alpha(N_0 P_i + P_0 N_i) + 2\delta N_0 N_i$$

$$+ \frac{\tilde{\epsilon}}{\kappa}(N_0 Q_i + Q_0 N_i) - N_i \qquad (5.4.9)$$

$$L_2(N_i, P_i, Q_i) \equiv D_0 P_i - \beta(P_0 Q_i + Q_0 P_i) + \gamma(1 + 3\kappa P_0^2)P_i \qquad (5.4.10)$$

$$L_3(N_i, P_i, Q_i) \equiv D_0 Q_i + a_0(Q_i - N_i) \qquad (5.4.11)$$

The source terms $S_{i,j}$ for $i = 1, 2$ and $j = 1, 2, 3$, i.e. at $O(\epsilon)$ and $O(\epsilon^2)$, are

$O(\epsilon):$

$$S_{1,1} = 0 \qquad (5.4.12)$$

$$S_{1,2} = 0 \qquad (5.4.13)$$

$$S_{1,3} = 0 \qquad (5.4.14)$$

$O(\epsilon^2):$

$$S_{2,1} = -D_1 N_1 - \delta N_1^2 - \alpha N_1 P_1 - \frac{\tilde{\epsilon}}{\kappa}N_1 Q_1 \qquad (5.4.15)$$

$$S_{2,2} = -D_1 P_1 + \beta P_1 Q_1 - 3\gamma\kappa P_0 P_1^2 \qquad (5.4.16)$$

$$S_{2,3} = -D_1 Q_1 + a_1(N_1 - Q_1). \qquad (5.4.17)$$

Now, we can use equation (5.4.7) to solve for $Q_i$ in terms of $P_i$. Also we can

solve (5.4.8) for $N_i$ in terms of $Q_i$. Then, we can use both of these results in (5.4.6)

76

to find the composite equation below.

$$L_c P_i = \Gamma_i \tag{5.4.18}$$

$$L_c = L_{c3} D_0^3 + L_{c2} D_0^2 + L_{c1} D_0 + L_{c0} \tag{5.4.19}$$

$$L_{c0} = \frac{1}{\beta \kappa P_0} (-2\beta(\epsilon + \delta + \kappa)N_0^2 + \gamma \kappa(\alpha P_0 - 1)(1 + e\kappa P_0^2)$$

$$+ N_0(\beta \kappa + 2\gamma(\epsilon + \delta \kappa)6\gamma \kappa(\epsilon + \delta \kappa)P_0^2)) \tag{5.4.20}$$

$$L_{c1} = \frac{1}{a_0 \beta \kappa P_0} (-\beta(\epsilon + 2\delta \kappa)N_0^2 + N_0(\epsilon \gamma + \beta \kappa + 2\gamma \delta \kappa + a_0(2\epsilon$$

$$- \beta \kappa + 2\delta \kappa) + \kappa P_0(-\alpha \beta + 3\gamma(\epsilon + 2\delta \kappa)P_0)) + \kappa(a_0(\gamma - 1)$$

$$- \gamma + P_0(\alpha(a_0 + \gamma) + 3\gamma \kappa P_0(a_0 - 1\alpha P_0)))) \tag{5.4.21}$$

$$L_{c2} = \frac{1}{a_0 \beta \kappa P_0} ((\epsilon - \beta \kappa + 2\delta \kappa)N_0 + \kappa(a_0 - 1 + \gamma + P_0(\alpha + 3\gamma \kappa P_0))) \tag{5.4.22}$$

$$L_{c3} = \frac{1}{a_0 \beta p_0} \tag{5.4.23}$$

$$\Gamma_i = S_{i,1} + \frac{2(\epsilon + \delta \kappa)N_0 + \kappa(\alpha P_0 - 1)}{\beta \kappa P_0} S_{i,2}$$

$$+ \frac{(\epsilon + 2\delta \kappa)N_0 + \kappa(\alpha P_0 - 1)}{a_0 \kappa} S_{i,3}$$

$$+ \frac{(\epsilon + 2\delta \kappa)N_0 + \kappa(a_0 - 1 + \alpha P_0)}{a_0 \beta \kappa P_0} D_0 S_{i,2}$$

$$+ \frac{1}{a_0} D_0 S_{i,3} + \frac{1}{a_0 \beta P_0} D_0^2 S_{i,2} \tag{5.4.24}$$

Now, we will use (5.4.18) to identify and suppress the secular terms in the solutions of (5.4.6)-(5.4.8).

We will find the solutions of the above equations (5.4.6)-(5.4.8). For $i = 1$, (5.4.12)-(5.4.14) show that $S_{1,1} = S_{1,2} = S_{1,3} = 0$. And so we will pick a solution for the first order population $P_1$.

$$P_1 = c_1(T_1, T_2)e^{\lambda_1 t} + c_2(T_1, T_2)e^{\lambda_2 t} + c_3(T_1, T_2)e^{\lambda_3 t} \tag{5.4.25}$$

Here $c_2 = \bar{c}_1$ is the complex conjugate of $c_1$ since $\lambda_2 = \bar{\lambda}_1$ and $P_1$ is a real valued function.

Note that since $\lambda_3 = 0$ and $P_1$ is real, $c_3$ is a real number.

$$c_3(T_1, T_2)e^{\lambda_3 t} = c_3(T_1, T_2) \tag{5.4.26}$$

Using (5.4.25) and (5.4.26) in (5.4.6)-(5.4.8) for $i = 1$ together with (5.4.12)-(5.4.14) gives us the values of the other first-order fields $N_1$ and $Q_1$.

Armed with the first-order solutions $N_1$, $P_1$ and $Q_1$, we may evaluate the second-order sources $S_{2,1}$ through $S_{2,3}$ using (5.4.15)-(5.4.17). Setting the coefficients of the secular $e^{\lambda_{1,2} t}$ terms in these sources (which are the solutions of the homogeneous equations for $i = 1$) to zero yields the normal form.

$$\frac{\partial c_1}{\partial T_1} = k_1 a_1 c_1 + k_2 c_1 c_3 \tag{5.4.27}$$

$$\frac{\partial c_3}{\partial T_1} = k_3 c_3^2 + k_4 c_1 c_2 \tag{5.4.28}$$

Here $k_1 - k_4$ are constants dependent upon our parameters, which are of the form

$$k_j = k_{jr} + i k_{ji}. \tag{5.4.29}$$

Writing $c_1 = Ae^{i\theta}$, the real and imaginary parts of (5.4.27) yield

$$\frac{\partial A}{\partial T_1} = k_{1r}a_1 A + k_{2r}c_3 A \tag{5.4.30}$$

$$A\frac{\partial \theta}{\partial T_1} = k_{1i}a_1 A + k_{2i}c_3 A. \tag{5.4.31}$$

The fixed points of (5.4.28) and (5.4.31) yield

$$c_3 = c_{3_c} = -\frac{k_{1r}}{k_{2r}}a_1 \tag{5.4.32}$$

$$A = A_c = \sqrt{\frac{-k_{1r}^2 k_3 a_1^2}{k_4 k_{2r}^2}}. \tag{5.4.33}$$

Using these values in the first-order fields yields the post-generalized Hopf periodic

orbits.

$$P_1 = \left(A_c e^{i\theta} e^{i\lambda_1 t} + A_c e^{-i\theta} e^{-i\lambda_1 t}\right) + c_{3_c}$$

$$= 2A_c \cos(\lambda_1 t + \theta) + c_{3_c} \tag{5.4.34}$$

The evolution and stability of the periodic orbit (5.4.34) of amplitude $A_c$ is governed

by (5.4.30) and (5.4.31). In particular, the stability of the periodic solution depends

on the stability of the fixed point $A_c$ of (5.4.30). To determine the stability, we com-

pute the Jacobian (and eigenvalue, as this is a one-dimensional system) of (5.4.30)

at $A = A_c$, $c_3 = c_{3_c}$, where the last step follows from (5.4.32).

$$J = \frac{\partial}{\partial A} \left( k_{1r} a_1 A + k_{2r} c_3 A \right) |_{A_c, c_{3_c}}$$

$$= k_{1r} a_1 + k_{2r} c_{3_c}$$

$$= 0$$

Since this eigenvalue is non-hyperbolic, or has zero real part, our linearized stability analysis of the periodic orbits (5.4.34) is inconclusive. Hence, we shall determine this via direct numerical simulations on (5.2.13) in the post-generalized-Hopf regime.

To this end, we consider actual parameter sets for the occurrence of the generalized Hopf bifurcation and the subsequent dynamics in the next section.

## 5.5    Numerical results

Supercritical generalized Hopf bifurcations give rise to a stable or attracting periodic orbit. By contrast, the subcritical generalized Hopf bifurcations correspond to an unstable periodic orbit coexisting with a stable fixed point for $a < a_0$. The unstable periodic orbit tightens like a noose around the fixed point as $a \rightarrow a_0^-$. At $a = a_0$, the two collide, causing the fixed point $(N_0, P_0, Q_0)$ to go unstable for $a = a_0^+$. Thus, there is neither a stable fixed point attractor nor a stable limit cycle attractor for $a = a_0^+$. Instead, there may be one of three possible dynamical behaviors at $a = a_0^+$:

(a) bounded quasiperiodic dynamics,

(b) bounded chaotic dynamics, or

(c) an attractor at infinity (a movable, initial-condition dependent singularity [24]) reached in a finite time.

However, in this chapter we are interested in degenerate Hopf bifurcations which do not satisfy the "simple eigenvalue hypothesis" that two of the eigenvalues are purely imaginary and the other has a nonzero real part, and so we should not expect the standard Hopf bifurcation diagrams to describe the behavior we see on either side of the bifurcation point.

And so, we now move on to numerical solutions. To proceed, we need values for the fixed point and for the bifurcation point $a_0$ of the control parameter. Physically relevant parameter values would be small and positive, since they represent growth, death, and predation rates and ratios between them. Figure 5.1 shows the coefficients of the characteristic polynomial $b1$, $b2$, and $b3$ plotted for small positive parameter values. It can be seen that $b1$ and $b3$ are always positive. Similar numerical and algebraic experiments indicate that these bifurcation conditions do not exist for physically relevant parameter values.
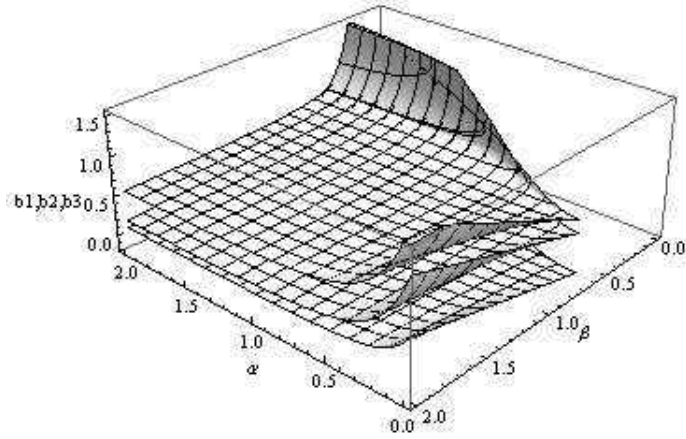
Figure 5.1: $b1$, $b2$ and $b3$ for $\kappa = 0.2$, $a = 0.5$, $e = 0.4$, $\gamma = 0.3$, $\delta = 0.4$.

For the purpose of this analysis, we will consider two cases corresponding to the following sets of numerical values:

$$\tilde{\epsilon} = 427.25, \quad \alpha = -0.237274, \quad \beta = -4096, \quad \delta = 29, \quad \gamma = -17, \quad \kappa = 2;$$

$$(5.5.1)$$

$$\tilde{\epsilon} = 36.0002, \quad \alpha = 1.69443, \quad \beta = 0.00488281, \quad \delta = 9, \quad \gamma = -25, \quad \kappa = -4.$$

$$(5.5.2)$$

Both of these parameter sets give positive values for the population of predator and prey at the fixed point.

82

For (5.5.1), the fixed point and bifurcation value is given below.

$$(N_0, P_0, Q_0) \approx (0.00417919, 0.0589068, 0.00417919) \tag{5.5.3}$$

The bifurcation value is given below.

$$a_0 \approx 0.114764. \tag{5.5.4}$$

Furthermore, from (5.3.5)-(5.3.7), the values of $\lambda$ are:

$$\lambda_{1,2} = \pm 0.246355i, \quad \lambda_3 = 0. \tag{5.5.5}$$

The corresponding values for (5.5.2) are

$$(N_0, P_0, Q_0) \approx (11605.3, 0.903696, 11605.3) \tag{5.5.6}$$

$$a_0 \approx -104611 \tag{5.5.7}$$

$$\lambda_{1,2} = \pm 169.991, \lambda_3 = 0. \tag{5.5.8}$$

In the case of a regular Hopf bifurcation in three dimensions, one pair of eigenvalues of the Jacobian matrix evaluated at the fixed point are complex conjugates with zero real parts, and the other eigenvalue is free. This free eigenvalue is also the trace of the matrix since the other two sum to zero, and so its value determines the dissipativity of the system. A large negative trace would be desirable to find bounded chaotic behavior. In the case of a generalized Hopf bifurcation in three dimensions, the third eigenvalue is zero, and so the trace is also zero.

For parameter set (5.5.1), we begin integrating at $(x_0 + ic\delta, y_0 + ic\delta, z_0 + ic\delta)$ where $ic\delta = 10^{-3}$. Figure 5.2 shows a stable fixed point on one side of the bifurcation. On the other side of the bifurcation, figure 5.3 shows periodic oscillations. In figure 5.4, the bifurcation parameter has moved farther away from the bifurcation point, and the periodic orbit has become unstable.

For the parameter set (5.5.2), we begin integrating at $(x_0 + ic\delta, y_0 + ic\delta, z_0 + ic\delta)$ where $ic\delta = 10^{-5}$. On one side of the bifurcation, in Figure 5.5, the system approaches a stable fixed point. On the other side of the bifurcation, in figure 5.6, a complicated attractor is created. In figure 5.7, we zoom in to the $t$ interval $(8000, 8250)$ to see the chaotically changing envelope of oscillations. The 3D parametric plot, shown in figure 5.8, shows trajectories orbiting a fixed point with a chaotically changing radius.

In order to confirm this and further characterize the suspected chaotic solutions, we employ the standard numerical diagnostics [24, 26–33] i.e., the power spectral density, the autocorrelation function, and the fractal dimensions (notice that one could also calculate Lyapunov exponents which measure the rate of divergence of neighboring trajectories on an attractor). The power spectral density and autocorrelation function of $N(t)$ are computed using codes from "Numerical Recipes in C" [25].
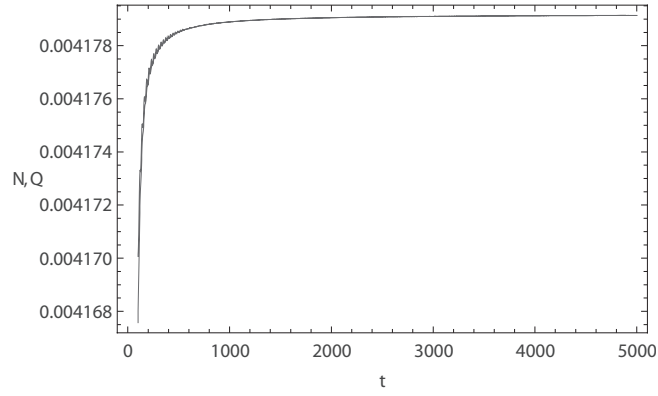
Figure 5.2: $N(t)$ and $Q(t)$ for $a_0 + 0.01$
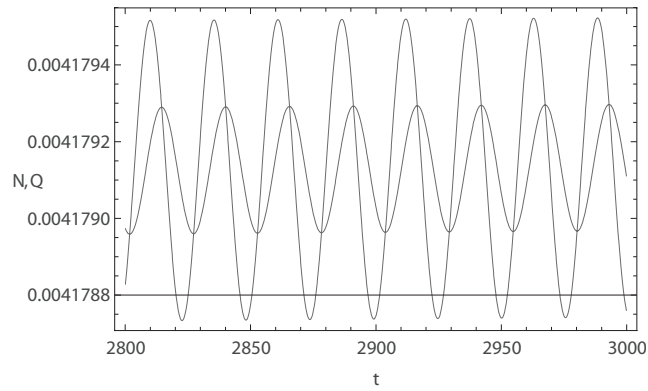


Figure 5.3: $N(t)$ and $Q(t)$ for $a_0 - 0.0001$
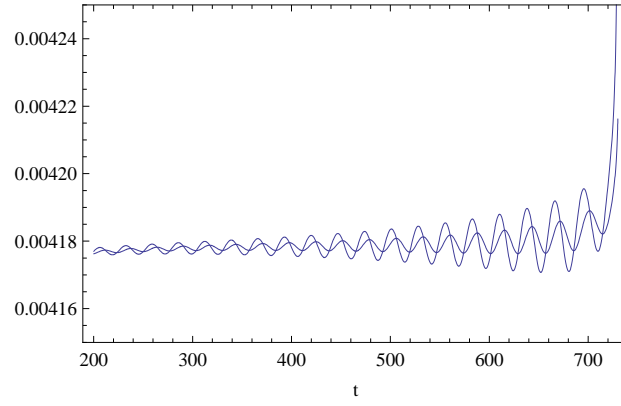
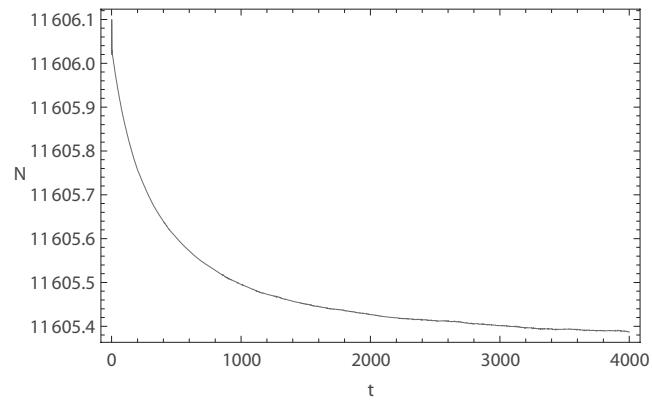Figure 5.4: $N(t)$ and $Q(t)$ for $a_0 - 0.01$



Figure 5.5: $N(t)$ for $a_0 - 0.1$

86
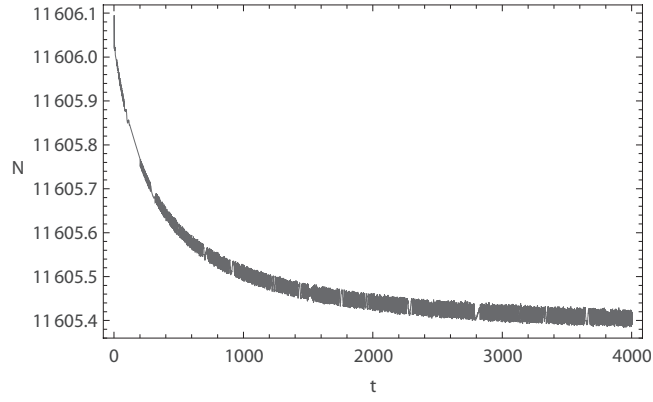
Figure 5.6: $N(t)$ for $a_0 + 0.1$
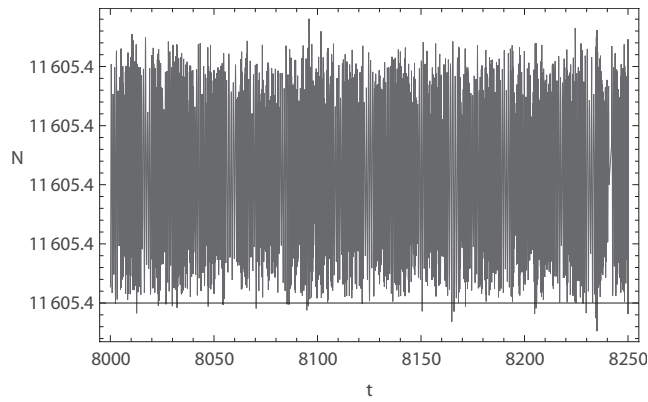


Figure 5.7: $N(t)$ plotted for $8000 < t < 8250$ and $a_0 + 0.1$
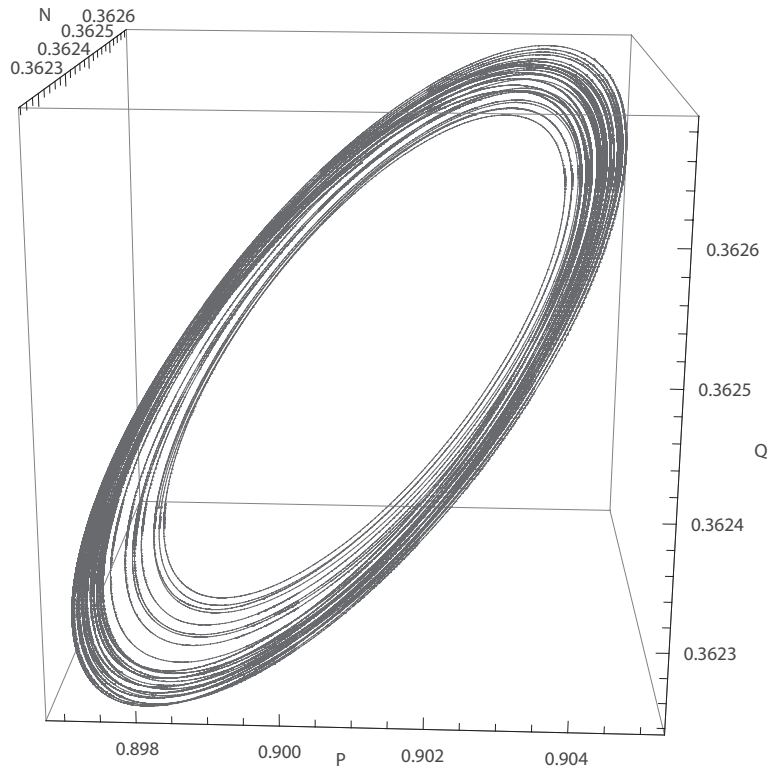
Figure 5.8: 3D Parametric Plot. The three variables have been scaled and translated to make the motion easier to see. The orbits are circling periodically, but the radius is changing chaotically.
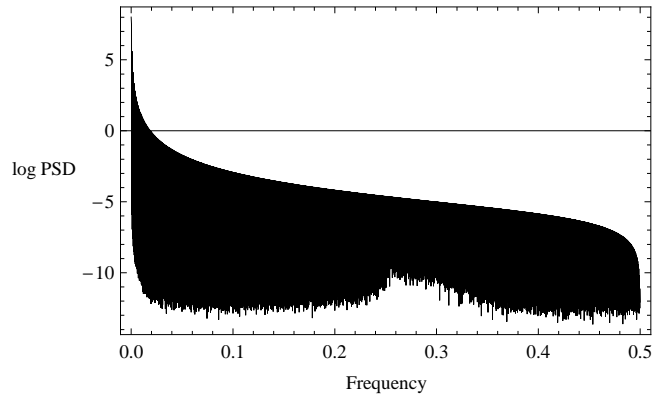
Figure 5.9: Power spectrum for $N(t)$ with perturbation $a_0 - 10^{-3}$. Broad features show lots of contributing frequencies which indicates chaos.
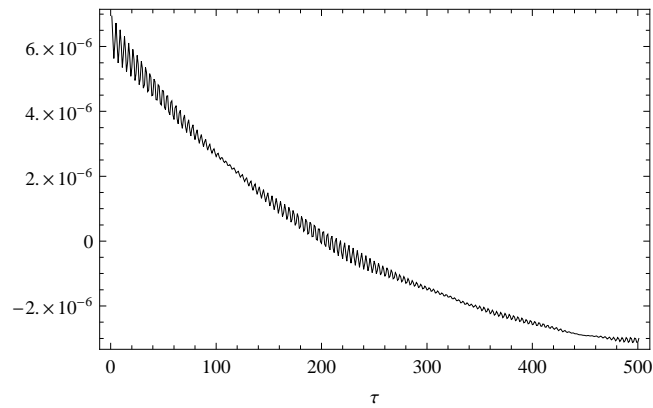


Figure 5.10: Autocorrelation function for $N(t)$ for $a_0 - 0.001$. The autocorrelation function goes to zero in a finite time, which is indicative of chaos. Its first zero is at about $\tau = 200$, which will be used as the delay in the cluster dimension calculation.

89
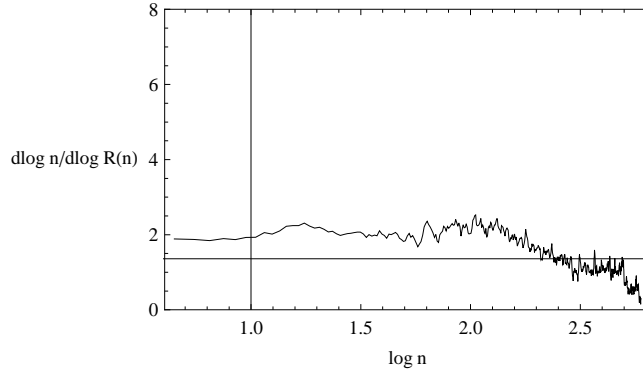
Figure 5.11: The best fit horizontal line is shown at $\mathrm{d}\log n/\mathrm{d}\log R(n) = 1.36$.

The broad features in the power spectral density in Figure 5.9 show that power is being injected into many different frequencies, which is indicative of chaos. The autocorrelation function first goes to zero at $t_c = 200$. This is used as the time delay in the fractal dimension calculation [24–35] which is discussed below.

A more quantitative and definitive numerical diagnostic is the fractal dimension. Strong randomness or stochastic behavior with many degrees of freedom can be distinguished from low-dimensional (deterministic) chaos by computing the fractal cluster dimension. Of several possible alternative definitions for the fractal dimension [24–35] we employ the cluster fractal dimension $D$ of Termonia and Alexandrowicz [29] which is defined below and where $R(n)$ is the average radius of an $E$-dimensional ball containing $n$ points.

$$n = k[R(n)]^D, \quad n \to \infty, \tag{5.5.9}$$

Thus, $D$ is the slope of a plot of $\log n$ versus $\log R(n)$. More usefully, if a scaling law (5.5.9) exists, then it would show up on a plot of $\mathrm{d}\log n/\mathrm{d}\log R(n)$ versus $\log n$, with the height of the line being a measure of $D$. Numerical computation of $D$ is somewhat subtle, and requires the embedding of the numerical time-series $N(t)$ in $E$-dimensional space with various values of $E$, via the construction (from $N(t)$) of "$E$-tuples"

$$[N(t), N(t+\tau), N(t+2\tau), \ldots, N(t+(E-1)\tau)], \tag{5.5.10}$$

$$[N(t+\tau), N(t+2\tau), \ldots, N(t+E\tau)], \ldots \tag{5.5.11}$$

This is a consequence of the Takens embedding theorem [24–35]. For each choice of embedding dimension $E$, the "delay" $\tau$ is typically chosen to be $t_c$, $t_c/2$ and $2t_c$ and $D$ is estimated for each $\tau$ from the slope of a $\log n/\log R(n)$ plot (provided this is approximately a straight line, or there is a well-defined scaling region) or the height of an approximate horizontal line in a $(\mathrm{d}\log n/\mathrm{d}\log R(n))/\log n$ plot. This is repeated for increasing $E$ until the estimates for $D$ saturate, which yields the converged estimate for $D$ (provided well-defined straight lines or scaling regions (5.5.9) occur in the plots and the $D$ values obtained for $\tau = t_c, t_c/2$, and $2t_c$ are in good agreement). Following this procedure, a sample plot is shown in Figure 5.11.

Figure 5.11 shows the $(\mathrm{d}\log n/\mathrm{d}\log R(n))/\log n$ plot for $E = 3$, $t_c = \tau$. From the height of the approximate horizontal line (which indicates a well-defined scaling

region), we can estimate the converged cluster fractal dimension to be a non-integer value in the range $D \in (1.3, 1.4)$. This confirms that the system possesses bounded low-dimensional (deterministic) chaotic solutions evolving on a strange attractor with fractal dimension $D \in (1.3, 1.4)$.

## 5.6    Conclusion

In conclusion, we have comprehensively analyzed generalized Hopf bifurcations and the resulting dynamics in our model predator-prey system both analytically and numerically. Both supercritical and subcritical bifurcations occur. However, in contrast to regular Hopf bifurcations [36], there is now the additional constraint that the sum of the eigenvalues at the point(s) of bifurcation is strictly zero. Since this is also the trace of the Jacobian matrix of the fixed point at bifurcation, and thus a measure of the system's relative rate of local volume contraction or dissipation, strong dissipativity is precluded at or near parameter sets corresponding to generalized Hopf bifurcation. Thus, even in subcritical cases, where there are no local (point or periodic) attractors in the post-bifurcation regime, the system is much more likely to fly off to attractors at infinity than for parameters corresponding to subcritical cases or the regular Hopf bifurcation. For the latter, strong dissipativity often precludes such blow-up and provides the folding part of the repeated 'stretching and folding'

mechanisms which makes bounded chaotic dynamics far more common than for the generalized Hopf cases.

**Part IV**

# DYNAMICAL CONSEQUENCES OF DOUBLE HOPF BIFURCATIONS

# CHAPTER 6
# PERIODIC AND QUASIPERIODIC WAVETRAINS FROM DOUBLE HOPF BIFURCATIONS IN PREDATOR-PREY SYSTEMS WITH GENERAL NONLINEARITIES

## 6.1 Abstract

Traveling wavetrains in generalized two-species predator-prey models and two-component reaction-diffusion equations are considered. The stabilities of the fixed points of the traveling wave ODEs (in the usual spatial variable) are found. For general functional forms of the nonlinear prey birthrate/deathrate or reaction terms, Hopf bifurcations are shown to occur at various critical values of the parameters. The post-bifurcation dynamics is investigated for three different functional forms of the nonlinearities. The normal forms near the double Hopf points are derived using the method of multiple scales. The possible post-bifurcation dynamics resulting from the normal form comprises stable limit cycles and 2-period tori corresponding to periodic and quasiperiodic wavetrains. In principle, subcritical Hopf bifurcations may yield more complex behavior, although none has been observed. The diverse behaviors predicted

95

from the normal forms in various parameter regimes are validated using numerical simulations and diagnostics.

## 6.2  Introduction

Morphogenesis, which is the occurrence of spatial form and pattern evolving from a spatially homogeneous state, is a fundamental problem in developmental biology. A seminal contribution to this problem was made by Turing [50] who studied reaction-diffusion equations of the form

$$
\begin{aligned}
\frac{\partial N}{\partial t} &= R_1(N, P) + D_1 \frac{\partial^2 N}{\partial x^2} \\
\frac{\partial P}{\partial t} &= R_2(N, P) + D_2 \frac{\partial^2 P}{\partial x^2}
\end{aligned}
\tag{6.2.1}
$$

In [50], the reaction functions (or kinematic terms) $R_1$ and $R_2$ were polynomials. However, the fundamental and somewhat surprising result that diffusion could destabilize an otherwise stable equilibrium leading to nonuniform spatial patterns (referred to as prepattern) is not dependent on particular forms of $R_1$ and $R_2$.

The Turing instability in reaction-diffusion models thus provided a plausible and robust mechanism for the establishment of spatial prepattern, which could then generate biological patterns for gene activation. Numerous extensions and applications followed. These include early theoretical and analytical extensions [50–52]. In par-

96

ticular, Segel and Jackson [53] showed that spatial patterns may occur via Turing instability in macroscopic (extended Lotka-Volterra) models in population biology as well, particularly for species dispersing at different rates. They also provided a lucid biology as well, particularly for species dispersing at different rates. They also provided a lucid physical explanation of how diffusion could indeed generate instability, contrary to its usual interpretation as a smoothing mechanism. Applications in developmental biology were stimulated by the work of Meinhards and Gierer [54–56], primarily consisting of numerical simulations of reaction-diffusion systems in various geometries. Analytical work has confirmed and extended the results of [54–56], including bifurcation analysis and investigations of nonstationary (traveling-wave) patterns, spirals, solitary peaks, and fronts [57–61]. These are reviewed in [62]. Other work has focused on explaining the properties of spatial patterns [63–66] on the basis of chemical interactions and geometric considerations. Alternative explanations of pattern-forming, not based on reaction-diffusion equations and the Turing mechanism have been investigated [67]. Recent reviews of these and other related work on spatial pattern forming are given by Levin and Siegel [68], Murray [47], and Edelstein-Keshet [69].

In order to incorporate various realistic physical effects which may cause at least one of the physical variables to depend on the past history of the system, it is

often necessary to introduce time-delays into the governing equations. Factors that introduce time lag may include age structure of the populations (influencing the birth and death rate), maturation periods (thresholds), feeding times and hunger coefficients in predator-prey interactions, reaction times, food storage times, and resource generation times. Models incorporating time delays in diverse spatially-homogeneous biological systems are extensively reviewed by MacDonald [39], and in the context of predator-prey models, by Cushing [37]. These include continuous models such as the Kolmogorov, May, Holling, Hsu, Leslie and Caperon models, as well as discrete models.

Consider (6.2.1) for the general two-species predator-prey model [49] with the reaction terms given below.

$$R_1(N, P) = NF(N) - \alpha NP - \frac{\tilde{\epsilon}N^2}{k} \tag{6.2.2}$$

$$R_2(N, P) = -PG(P) + \beta NP$$

Here $N(t)$ and $P(t)$ are the prey and predator populations, respectively, $\tilde{\epsilon}$ is the birth rate of the prey, $k > 0$ is the carrying capacity, $\alpha$ is the rate of predation per predator, and $\beta$ is the rate of the prey's contribution to predator growth.

In this paper, we initiate a fresh and detailed investigation of traveling spatial wave patterns of (6.2.1) in the following form.

$$N(x,t) = N(\zeta) \tag{6.2.3}$$

$$P(x,t) = P(\zeta)$$

Here $\zeta = x - vt$ is the traveling wave, or "spatial" variable, and $v$ is the translation or wave speed. Substitution of Eqns (6.2.3) and (6.2.2) in (6.2.1) leads, after some simplification, to the following four-mode dynamical system.

$$\dot{N} = M \tag{6.2.4}$$

$$\dot{M} = \frac{1}{D_1}\left(-vM - NF(N) + \alpha NP + \frac{\theta N^2}{z}\right)$$

$$\dot{P} = Q$$

$$\dot{Q} = \frac{1}{D_2}\left(-vQ + PG(P) - \beta NP\right)$$

Here $F(N)$ and $G(P)$ are certain functions unique to each system.

While there have been a very large number of studies of regular Hopf bifurcations, generalized and degenerate Hopf bifurcations are far less widely studied. Among recent comprehensive treatments, we may list the monograph by Huseyin [3], the thesis by Planeaux [4], and the review by Yu [5], as well as the comprehensive reference lists in all three. The first named is reasonably comprehensive at the analytical end but employs the little-used generalized Harmonic Balance asymptotic

99

analysis technique. By contrast, [51] is a comprehensive numerical analysis in the context of chemical reactor dynamics. Ref [52] uses a mix of analytic techniques and limited numerical simulations to consider the dynamics resulting from generalized and degenerate Hopf bifurcations.

Here we will follow [62] and especially [5] to consider the stability of the equilibria and the double Hopf bifurcations of 6.2.4 for general functions $F(N)$ and $G(P)$. We will derive the normal form governing the post-bifurcation dynamics and the possible post-bifurcation dynamics in various parameters is deduced from it. The resulting predictions will be matched against numerical simulations and diagnostics.

## 6.3  Linear stability analysis

The fixed points of system (6.2.4) are

$$(N_0, M_0, P_0, Q_0) = \left( \frac{G(P_0)}{\beta}, 0, \frac{z\beta F(N_0) - \theta G(P_0)}{z\alpha\beta}, 0 \right). \tag{6.3.1}$$

The functions $F(N)$ and $G(P)$ are kept general during the analysis but are subsequently chosen to correspond to three systems analysed by Mancas [70].

A.  $F(N) = \rho, \ G(P) = \gamma, \ \theta = 0$ \hfill (6.3.2)

B.  $F(N) = \rho, \ G(P) = \gamma, \ \theta = \rho$ \hfill (6.3.3)

C.  $F(N) = k_0, \ G(P) = d + cP, \ \theta = \rho$ \hfill (6.3.4)

The Jacobian matrix of (6.2.4) at the fixed point $(N_0, M_0, P_0, Q_0)$ is

$$
J = \begin{bmatrix}
0 & 1 & 0 & 0 \\
\frac{G_0(-F_0'z+\theta)}{D_1 z\beta} & -\frac{v}{D_1} & \frac{\alpha G_0}{D_1\beta} & 0 \\
0 & 0 & 0 & 1 \\
\frac{-F_0 z\beta + G_0\theta}{D_2 z\alpha} & 0 & \frac{G_0'(F_0 z\beta - G_0\theta)}{D_2 z\alpha\beta} & -\frac{v}{D_2}
\end{bmatrix}.
\tag{6.3.5}
$$

Here $F_0 = F(N_0)$ and $G_0 = G(P_0)$. The eigenvalues $\lambda$ of (6.3.5) satisfy the characteristic equation below.

$$
\lambda^4 + b_1\lambda^3 + b_2\lambda^2 + b_3\lambda + b_4 = 0
\tag{6.3.6}
$$

Here $b_i$, $i = 1, \ldots, 4$ are given below.

$$
b_1 = \frac{(D_1 + D_2)v}{D_1 D_2}
$$

$$
b_2 = \frac{v^2}{D_1 D_2} - \frac{F_0 G_0'}{D_2\alpha} + \frac{F_0' G_0}{D_1\beta} - \frac{G_0\theta}{D_1 z\beta} + \frac{G_0 G_0'\theta}{D_2 z\alpha\beta}
$$

$$
b_3 = v\frac{F_0' G_0 z\alpha - F_0 G_0' z\beta + G_0\theta(G_0' - \alpha)}{D_1 D_2 z\alpha\beta}
$$

$$
b_4 = G_0\frac{(F_0 z\beta - G_0\theta)(-F_0' G_0' z + z\alpha\beta + G_0'\theta)}{D_1 D_2 z^2\alpha\beta^2}
$$

Presently we are interested in double Hopf bifurcations, so we want the four eigenvalues to be two pairs of purely imaginary complex conjugates. Hence we impose the characteristic form

$$
(\lambda^2 + \omega_1^2)(\lambda^2 + \omega_2^2) = 0
$$

$$
\lambda^4 + b_2\lambda^2 + b_4 = 0.
$$

This determines that the conditions for a double Hopf bifurcation are

$$b_1 = 0 \tag{6.3.7}$$

$$b_2 = \omega_1^2 + \omega_2^2 > 0 \tag{6.3.8}$$

$$b_3 = 0 \tag{6.3.9}$$

$$b_4 = \omega_1^2 \omega_2^2 > 0 \tag{6.3.10}$$

$$\omega_1, \omega_2 \in \mathbb{R} \tag{6.3.11}$$

## 6.4 Analytical construction of periodic orbits

We will use the method of multiple scales to contruct analytical approximations for the periodic orbits arising through the double Hopf bifurcation of the fixed point.

The multiple scales expansions take the following form.

$$\dot{N} = N_0 + \sum_{n=1}^{3} \epsilon^n N_n(T_0, T_1, T_2) + \ldots \tag{6.4.1}$$

$$\dot{M} = M_0 + \sum_{n=1}^{3} \epsilon^n M_n(T_0, T_1, T_2) + \ldots$$

$$\dot{P} = P_0 + \sum_{n=1}^{3} \epsilon^n P_n(T_0, T_1, T_2) + \ldots$$

$$\dot{Q} = Q_0 + \sum_{n=1}^{3} \epsilon^n Q_n(T_0, T_1, T_2) + \ldots$$

Here $T_n = \epsilon^n t$ and $\epsilon$ is a small positive non-dimensional parameter that distinguishes different time scales. The time derivative is shown below, where $\mathrm{D}_n = \partial/(\partial T_n)$.

$$\frac{\mathrm{d}}{\mathrm{d}t} = \mathrm{D}_0 + \epsilon \mathrm{D}_1 + \epsilon^2 \mathrm{D}_2 + \dots \tag{6.4.2}$$

The control parameters are expanded as $\tau_1 = T_1 + \epsilon^2 \mu_1$ and $\tau_2 = T_2 + \epsilon^2 \mu_2$. This allows the nonlinear terms and the control parameters to occur at the same order. We use $\tau_1 = D2$ and $\tau_2 = \beta$ in our calculations.

Using the expansions (6.4.1) in (6.2.4) and matching powers of $\epsilon$ yields equations of the following form.

$$L_1(N_i, M_i, P_i, Q_i) = S_{i,1} \tag{6.4.3}$$

$$L_2(N_i, M_i, P_i, Q_i) = S_{i,2} \tag{6.4.4}$$

$$L_3(N_i, M_i, P_i, Q_i) = S_{i,3} \tag{6.4.5}$$

$$L_4(N_i, M_i, P_i, Q_i) = S_{i,4} \tag{6.4.6}$$

Here the $L_i, \ i = 1, 2, 3, 4$ are the following differential operators.

$$L_1(N_i, M_i, P_i, Q_i) \equiv -M_i + \mathrm{D}_0 N_i \tag{6.4.7}$$

$$L_2(N_i, M_i, P_i, Q_i) \equiv \frac{vM_i}{D_1} - \frac{G_0 \theta N_i}{D_1 z \beta} - \frac{G_0 \alpha P_i}{D_1 \beta} + \mathrm{D}_0 M_i$$

$$L_3(N_i, M_i, P_i, Q_i) \equiv -Q_i + \mathrm{D}_0 P_i$$

$$L_4(N_i, M_i, P_i, Q_i) \equiv \frac{F_0 z \beta - G_0 \theta}{D_2 z \alpha} N_i + \frac{v}{D_2} Q_i + \mathrm{D}_0 Q_i$$

103

The source terms $S_{i,j}$ , $i = 1, 2, 3$ , $j = 1, 2, 3, 4$ are given in Appendix A. Equation (6.4.3) may be solved for $M_i$, (6.4.4) for $P_i$, and (6.4.5) for $Q_i$.

$$M_i = - S_{i,1} + D_0 N_i \tag{6.4.8}$$

$$P_i = \frac{v\beta}{G_0\alpha} M_i - \frac{\theta}{z\alpha} N_i - \frac{D_1\beta}{G_0\alpha} S_{i,2} + \frac{D_1\beta}{G_0\alpha} D_0 M_i \tag{6.4.9}$$

$$Q_i = - S_{i,3} + D_0 P_i \tag{6.4.10}$$

These can be plugged into (6.4.6) in the order (6.4.10), (6.4.9), (6.4.8) to obtain the following composite equation.

$$L_c N_i = \Gamma_i \tag{6.4.11}$$

The composite operator $L_c$ and $\Gamma_i$ are given in Appendix A.

To find the solutions of (6.4.3)-(6.4.6), we note that $S_{1,i} = 0$ for $i = 1, 2, 3, 4$ and so we choose the following first order solution.

$$N_1 = \alpha(T_1, T_2)e^{i\omega_1 T_0} + \bar{\alpha}(T_1, T_2)e^{-i\omega_1 T_0} \tag{6.4.12}$$

$$+ \beta(T_1, T_2)e^{i\omega_2 T_0} + \bar{\beta}(T_1, T_2)e^{-i\omega_2 T_0}$$

The fields $\alpha$ and $\beta$ correspond to the center manifold where $\omega_1$ and $\omega_2$ are real. Using (6.4.12) in (6.4.8)-(6.4.10) with $i = 1$ yields the other first order fields $M_1, P_1, Q_1$. With the first order fields known, the second order source $\Gamma_2$ may be evaluated. Suppressing secular source terms (solutions of the homogeneous equations for $i = 1$)

gives the requirement

$$\frac{\mathrm{d}\alpha}{\mathrm{d}T_1} = \frac{\mathrm{d}\bar{\alpha}}{\mathrm{d}T_1} = \frac{\mathrm{d}\beta}{\mathrm{d}T_1} = \frac{\mathrm{d}\bar{\beta}}{\mathrm{d}T_1} = 0. \tag{6.4.13}$$

Now we assume a second order solution of the form

$$\begin{aligned}
N_2 =& N_{200} + N_{201}\alpha(T_2)\bar{\alpha}(T_2) + N_{202}\beta(T_2)\bar{\beta}(T_2) \\
&+ N_{203}\alpha(T_2)^2 e^{2i\omega_1 T_0} + N_{204}\bar{\alpha}(T_2)^2 e^{-2i\omega_1 T_0} \\
&+ N_{205}\beta(T_2)^2 e^{2i\omega_2 T_0} + N_{206}\bar{\beta}(T_2)^2 e^{-2i\omega_2 T_0} \\
&+ N_{207}\alpha(T_2)\beta(T_2) e^{i(\omega_1+\omega_2)T_0} + N_{208}\alpha(T_2)\bar{\beta}(T_2) e^{i(\omega_1-\omega_2)T_0} \\
&+ N_{209}\bar{\alpha}(T_2)\beta(T_2) e^{-i(\omega_1-\omega_2)T_0} + N_{210}\bar{\alpha}(T_2)\bar{\beta}(T_2) e^{-i(\omega_1+\omega_2)T_0} \tag{6.4.14}
\end{aligned}$$

This solution is plugged into (6.4.11) with $i = 2$. Coefficients of exponentials with identical arguments on either side are matched to determine $N200, N201, \ldots, N210$.

Evaluating the third order source term $\Gamma_3$ with the first and second order solutions and setting first order harmonics equal to zero produces the normal form.

$$\alpha'(T_2) = c_1\alpha(T_2)\beta(T_2)\bar{\beta}(T_2) + c_2\alpha(T_2)^2\bar{\alpha}(T_2) + c_3\alpha(T_2) \tag{6.4.15}$$

$$\beta'(T_2) = c_4\alpha(T_2)\bar{\alpha}(T_2)\beta(T_2) + c_5\beta(T_2)^2\bar{\beta}(T_2) + c_6\beta(T_2)$$

Note that $c_1$ through $c_6$ are complex. We can more easily find periodic orbits by switching to polar coordinates.

$$\alpha(T_2) = \rho_1(T_2)e^{i\theta_1(T_2)} \tag{6.4.16}$$

$$\bar{\alpha}(T_2) = \rho_1(T_2)e^{-i\theta_1(T_2)}$$

$$\beta(T_2) = \rho_2(T_2)e^{i\theta_2(T_2)}$$

$$\bar{\beta}(T_2) = \rho_2(T_2)e^{-i\theta_2(T_2)}$$

Plugging (6.4.16) into (6.4.15) and separating real and imaginary parts of the resulting equations gives the normal form in polar coordinates.

$$\rho_1'(T_2) = \rho_1(T_2)\left(\mathrm{Re}[c_3] + \mathrm{Re}[c_2]\rho_1(T_2)^2 + \mathrm{Re}[c_1]\rho_2(T_2)^2\right) \tag{6.4.17}$$

$$\rho_2'(T_2) = \rho_2(T_2)\left(\mathrm{Re}[c_6] + \mathrm{Re}[c_4]\rho_1(T_2)^2 + \mathrm{Re}[c_5]\rho_2(T_2)^2\right) \tag{6.4.18}$$

$$\theta_1'(T_2) = \mathrm{Im}[c_3] + \mathrm{Im}[c_2]\rho_1(T_2)^2 + \mathrm{Im}[c_1]\rho_2(T_2)^2$$

$$\theta_2'(T_2) = \mathrm{Im}[c_6] + \mathrm{Im}[c_4]\rho_1(T_2)^2 + \mathrm{Im}[c_5]\rho_2(T_2)^2$$

Re[$c_3$] and Re[$c_6$] are expressions which are both linear in the second order deviations $\mu_1$ and $\mu_2$. The normal form can be written

$$\rho_1'(T_2) = \rho_1(T_2)\left(\alpha_{11}\mu_1 + \alpha_{12}\mu_2 + a_{20}\rho_1(T_2)^2 + a_{02}\rho_2(T_2)^2\right) \qquad (6.4.19)$$

$$\rho_2'(T_2) = \rho_2(T_2)\left(\alpha_{21}\mu_1 + \alpha_{22}\mu_2 + b_{20}\rho_1(T_2)^2 + b_{02}\rho_2(T_2)^2\right) \qquad (6.4.20)$$

$$\theta_1'(T_2) = \omega_1 + \beta_{11}\mu_1 + \beta_{12}\mu_2 + c_{20}\rho_1(T_2)^2 + c_{02}\rho_2(T_2)^2$$

$$\theta_2'(T_2) = \omega_2 + \beta_{21}\mu_1 + \beta_{22}\mu_2 + d_{20}\rho_1(T_2)^2 + d_{02}\rho_2(T_2)^2$$

## 6.5    Predictions for Post-Bifurcation Dynamics and Comparisons with Numerical Simulations

We now analyze (6.4.19)/(6.4.20) for the possible dynamical behaviors. Note that the periodic and 2-period quasiperiodic behaviors which we shall find in various parameter regimes correspond to periodic and quasiperiodic wavetrains of (6.2.1)/(6.2.2).

Periodic solutions are found by setting (6.4.19) and (6.4.20) equal to zero and solving for $\rho_1(T_2)$ and $\rho_2(T_2)$.

There are four solutions: the inital equilibrium solution (6.5.1), the Hopf bifurcation solution with frequency $\omega_1$ (6.5.2), the Hopf bifurcation solution with frequency

$\omega_2$ (6.5.3), and the quasiperiodic solution with frequencies $\omega_1$ and $\omega_2$ (6.5.4).

$$\rho_1 = \rho_2 = 0 \tag{6.5.1}$$

$$\rho_1^2 = -\frac{1}{a_{20}}(\alpha_{11}\mu_1 + \alpha_{12}\mu_2), \quad \rho_2 = 0 \tag{6.5.2}$$

$$\rho_1 = 0, \quad \rho_2^2 = -\frac{1}{b_{02}}(\alpha_{21}\mu_1 + \alpha_{22}\mu_2) \tag{6.5.3}$$

$$\rho_1^2 = \frac{1}{a_{20}b_{02} - a_{02}b_{20}}[a_{02}(\alpha_{21}\mu_1 + \alpha_{22}\mu_2) - b_{02}(\alpha_{11}\mu_1 + \alpha_{21}\mu_2)] \tag{6.5.4}$$

$$\rho_2^2 = \frac{1}{a_{20}b_{02} - a_{02}b_{20}}[b_{20}(\alpha_{11}\mu_1 + \alpha_{12}\mu_2) - a_{20}(\alpha_{21}\mu_1 + \alpha_{22}\mu_2)]$$

The stability conditions for each of these solutions can be determined with the Jacobian of (6.4.19) and (6.4.20).

$$J = \begin{bmatrix} \alpha_{11}\mu_1 + \alpha_{12}\mu_2 + 3a_{20}\rho_1^2 + a_{02}\rho_1\rho_2 & 2a_{02}\rho_1\rho_2 \\ 2b_{20}\rho_1\rho_2 & \alpha_{21}\mu_1 + \alpha_{22}\mu_2 + b_{20}\rho_1^2 + 3b_{02}\rho_2^2 \end{bmatrix} \tag{6.5.5}$$

Evaluating (6.5.5) on the solution (6.5.1) reveals the stability conditions for the equilibrium solution:

$$\alpha_{11}\mu_1 + \alpha_{12}\mu_2 < 0 \quad \text{and} \quad \alpha_{21}\mu_1 + \alpha_{22}\mu_2 < 0 \tag{6.5.6}$$

Changing either of these inequalities to an equality produces a critical line where a family of limit cycles bifurcates from the equilibrium solution (6.5.1). The first critical line (6.5.7) supports limit cycles with the approximate solution (6.5.2). The

second critical line (6.5.8) supports limit cycles with the approximate solution (6.5.3).

$$L1: \quad \alpha_{11}\mu_1 + \alpha_{12}\mu_2 = 0 \quad \text{and} \quad \alpha_{21}\mu_1 + \alpha_{22}\mu_2 < 0 \tag{6.5.7}$$

$$L2: \quad \alpha_{11}\mu_1 + \alpha_{12}\mu_2 < 0 \quad \text{and} \quad \alpha_{21}\mu_1 + \alpha_{22}\mu_2 = 0 \tag{6.5.8}$$

Evaluating (6.5.5) on the Hopf bifurcation solution (6.5.3) yields the stability condi-

tions (6.5.9) and (6.5.10).

$$\alpha_{11}\mu_1 + \alpha_{12}\mu_2 > 0 \tag{6.5.9}$$

$$\alpha_{21}\mu_1 + \alpha_{22}\mu_2 - \frac{b_{20}}{a_{20}}(\alpha_{11}\mu_1 + \alpha_{12}\mu_2) < 0. \tag{6.5.10}$$

When $a_{20} < 0$, the above conditions also allow the Hopf bifurcation solution (6.5.2)

to exist. Changing the second inequality to an equality results in the third critical

line L3, along which a secondary Hopf bifurcation takes place with frequency $\omega_2$.

The trajectories trace out a 2-D torus described by (6.5.4).

$$L3: \quad \left(\alpha_{21} - \frac{b_{20}}{a_{20}}\alpha_{11}\right)\mu_1 + \left(\alpha_{22} - \frac{b_{20}}{a_{20}}\alpha_{12}\right)\mu_2 = 0 \tag{6.5.11}$$

$$\alpha_{11}\mu_1 + \alpha_{12}\mu_2 > 0$$

When $b_{02} < 0$, the conditions (6.5.12) allow the Hopf bifurcation solution (6.5.3) to

exist. Changing the second inequality to an equality results in the fourth critical line

L4, along which a secondary Hopf bifurcation takes place with frequency $\omega_1$. The

trajectories trace out the 2-D torus described by (6.5.4).

$$\alpha_{21}\mu_1 + \alpha_{22}\mu_2 > 0 \tag{6.5.12}$$

$$\alpha_{11}\mu_1 + \alpha_{12}\mu_2 - \frac{a_{02}}{b_{02}}(\alpha_{21}\mu_1 + \alpha_{22}\mu_2) < 0$$

$$\text{L4}: \quad \left(\alpha_{11} - \frac{a_{02}}{b_{02}}\alpha_{21}\right)\mu_1 + \left(\alpha_{12} - \frac{a_{02}}{b_{02}}\alpha_{22}\right)\mu_2 = 0 \tag{6.5.13}$$

$$\alpha_{21}\mu_1 + \alpha_{22}\mu_2 > 0$$

The stability conditions of the quasiperiodic solution (6.5.4) are fully derived in [5], and the resulting critical line L5, where a quasiperiodic solution loses stability and may bifurcate into a motion on a 3-D torus, is given here:

$$\text{L5}: \quad \left[a_{20}(a_{02} - b_{02})\alpha_{21} - b_{02}(a_{20} - b_{20})\alpha_{11}\right]\mu_1$$

$$+ \left[a_{20}(a_{02} - b_{02})\alpha_{22} - b_{02}(a_{20} - b_{20})\alpha_{12}\right]\mu_2 = 0 \tag{6.5.14}$$

The line L5 must satisfy the existence conditions- geometrically speaking, the line L5 must lie between the lines L3 and L4.

### 6.5.1  Systems A and B

The characteristic polynomial of the Jacobian (6.5.5) is

$$\lambda^4 + \left(\frac{1}{D_1} + \frac{1}{D_2}\right)v\lambda^3 + \frac{v^2}{D_1 D_2}\lambda^2 + \frac{\gamma\rho}{D_1 D_2} \tag{6.5.15}$$

110

The double Hopf conditions (6.3.7)-(6.3.11) reduce to

$$\left(\frac{1}{D_1} + \frac{1}{D_2}\right) v = 0 \tag{6.5.16}$$

$$\frac{v^2}{D_1 D_2} - \text{sgn}(\alpha)\sqrt{v^4 - 4D_1 D_2 \gamma \rho} > 0 \tag{6.5.17}$$

$$\frac{v^2}{D_1 D_2} + \text{sgn}(\alpha)\sqrt{v^4 - 4D_1 D_2 \gamma \rho} > 0 \tag{6.5.18}$$

These conditions are unable to be satisfied simultaneously. Therefore, we conclude

that systems A and B have no double Hopf bifurcations.

### 6.5.2  System C

The double Hopf conditions for system C are satisfied by the numerical values $\beta =$

20.8, $\alpha = 2.0245424389488$, $d = 19.8$, $\rho = -20.53280120743$, $v = 1$, $c = 13.8$,

$z = 2.8$, $k_0 = -9.2$, $D_1 = 1$, $D_2 = -1$. The coefficients of the normal form equations

(6.4.19) and (6.4.20) are

$$\alpha_{11} = 0.6678559485566$$

$$\alpha_{22} = -0.0873243655541$$

$$\alpha_{12} = 0.0873243655541$$

$$\alpha_{21} = -0.1678559485567$$

$$a_{02} = 317.3289342685$$

$$a_{20} = -27.52499854917$$

$$b_{02} = -158.6644671343$$

$$b_{20} = 55.0499970983$$

The bifurcations lines are

$$L1: \quad D22 + 0.52023396\beta2 = 0 \quad \text{and} \quad D22 + 0.13075329454\beta2 < 0 \qquad (6.5.19)$$

$$L2: \quad D22 + 0.520233964\beta2 > 0 \quad \text{and} \quad D22 + 0.13075329454\beta2 = 0 \qquad (6.5.20)$$

$$L3: \quad D22 + 0.07477323352\beta2 = 0 \quad \text{and} \quad D22 + 0.1307532945\beta2 > 0 \qquad (6.5.21)$$

$$L4: \quad D22 - 0.26291112297\beta2 = 0 \quad \text{and} \quad D22 + 0.520233964\beta2 < 0 \qquad (6.5.22)$$

$$L5: \quad D22 + 4.25185092759 * 10^{-14}\beta2 = 0 \qquad (6.5.23)$$

The bifurcations lines for system C are shown in Figure 6.1.

Choosing $\mu_1 = -0.24$ and $\mu_2 = 0.79$ between L1 and L2 results in the stable equilibrium solution shown in Figure 6.2.

The second order deviation values $\mu_1 = -0.4$ and $\mu_2 = 0.6$ place the sample point immediately after the line L1 where a Hopf bifurcation occurs, and the stable periodic orbit that is created is shown in Figure 6.3.

The values $\mu_1 = -0.11$ and $\mu_2 = 0.9$ place the sample point immediately after another Hopf bifurcation at L2, and the stable periodic orbit that is created is shown in Figure 6.4. In this case, we show the periodic oscillations of $N(t)$.

The values $\mu_1 = -0.06$ and $\mu_2 = 0.9$ place the sample point immediately after the line L3 where a static bifurcation of the periodic orbit occurs, and the quasi-periodic orbit that is created is shown in Figure 6.5. The power spectrum of this solution is shown in Figure 6.6. Two frequency peaks indicate quasiperiodic motion.

The values $\mu_1 = -0.15$ and $\mu_2 = -0.7$ place the sample point immediately after the line L4 where another Hopf bifurcation occurs, and the unstable solution that is created is shown in Figure 6.7. In this case, the solution flies off to infinity in finite time.

The values $\mu_1 = 0.02$ and $\mu_2 = 0.9$ place the sample point immediately after the line L5 where a secondary Hopf bifurcation of the stable quasiperiodic orbit occurs,
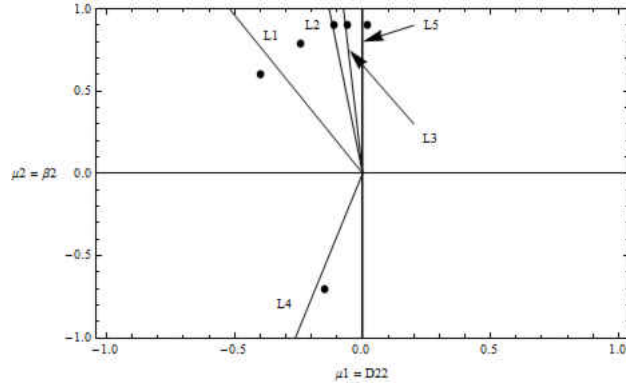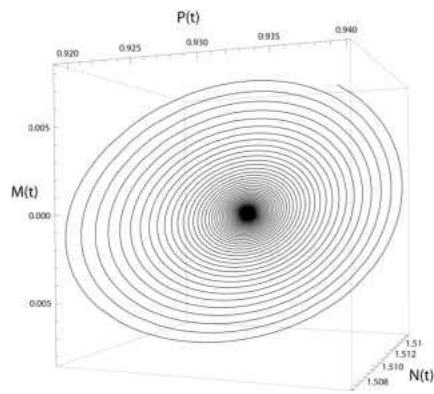
Figure 6.1: Bifurcation lines of system C



Figure 6.2: A stable fixed point exists in the region between the first two bifurcation lines L1 and L2.
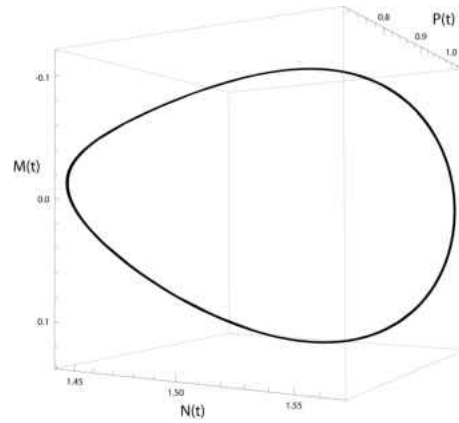
Figure 6.3: A stable periodic orbit is created during the first Hopf bifurcation.
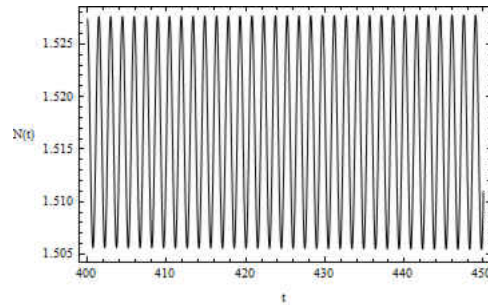


Figure 6.4: A stable periodic orbit is created during the first Hopf bifurcation.
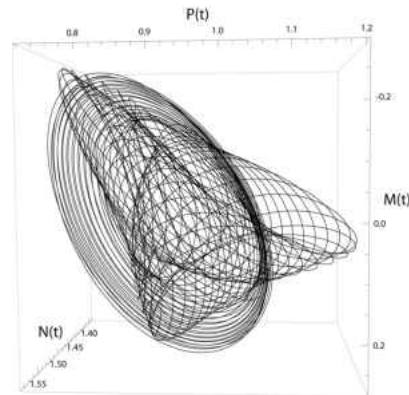


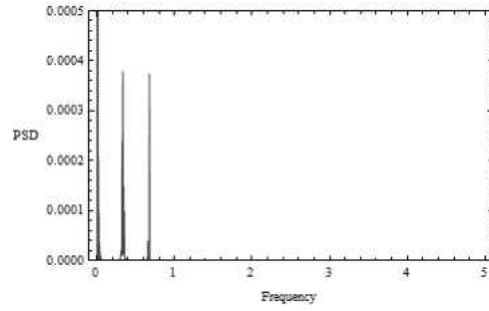Figure 6.5: A stable quasi-periodic orbit is created during the first Hopf bifurcation.

115

Figure 6.6: The power spectrum for the stable quasiperiodic orbit shows two clear peaks indicating that power is being concentrated in these distinct frequencies.
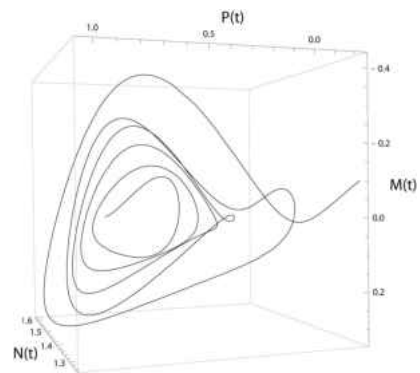


Figure 6.7: The solution in the region after L4 is unstable.

and the quasi-periodic orbit is now unstable. Trajectories fly to infinity soon after the interesting behavior shown in Figure 6.8.

## 6.6   Conclusion

We have comprehensively analyzed the wavetrain dynamics resulting from Hopf and double-Hopf bifurcations in two-reactant reaction-diffusion (or two-species predator-prey) systems with general nonlinearities. For general functional forms of the nonlinear prey birthrate/prey deathrate or reaction terms, regular/double-Hopf bifurcations are shown to occur at various critical values of the traveling wave speed. The post-bifurcation dynamics is investigated for three different functional forms of the nonlinearities. The normal forms near the double Hopf points have been derived using the method of multiple scales. The post bifurcation dynamics resulting from the normal form include stable limit cycles and two-period tori corresponding to periodic and quasiperiodic wave trains. In principle, subcritical Hopf bifurcations may yield more complex behavior, although none has been observed. The diverse behaviors predicted from the normal forms in various parameter regimes have been validated using numerical simulations and diagnostics. In general, the dynamics changes between analytically predicted regions of phase space separated by stability boundaries derived from the the normal form.

## 6.7    Appendix A

For systems A-C, the source terms are

$$S_{1,1} = S_{1,2} = S_{1,3} = S_{1,4} = 0 \tag{6.7.1}$$

$$S_{2,1} = -\,D_1 N_1 \tag{6.7.2}$$

$$S_{2,2} = \frac{F_0 G_0 \alpha_2}{D_1 \alpha \beta} - \frac{G_0^2 z_2 \theta}{D_1 z^2 \beta^2} - \frac{G_0^2 \alpha_2 \theta}{D_1 z \alpha \beta^2} + \frac{G_0^2 \theta_2}{D_1 z \beta^2} + \frac{\theta}{D_1 z} N_1^2$$

$$+ \frac{\alpha}{D_1} N_1 P_1 - D_1 M_1 \tag{6.7.3}$$

$$S_{2,3} = -\,D_1 P_1 \tag{6.7.4}$$

$$S_{2,4} = -\frac{F_0 G_0 \beta_2}{D_2 \alpha \beta} + \frac{G_0^2 \beta_2 \theta}{D_2 z \alpha \beta^2} - \frac{N_1 P_1 \beta}{D_2} + \frac{D_{22} q_0 v}{D_2^2} - \frac{q_0 v_2}{D_2} - D_1 Q_1 \tag{6.7.5}$$

$$S_{3,1} = -\,D_2 N_1 - D_1 N_2 \tag{6.7.6}$$

$$S_{3,2} = N_1 \left( \frac{F_0 \alpha_2}{D_1 \alpha} - \frac{2 G_0 z_2 \theta}{D_1 z^2 \beta} - \frac{G_0 \alpha_2 \theta}{D_1 z \alpha \beta} + \frac{2 D_1 G_0 \theta_2 - D_{12} G_0 \theta}{D_1^2 z \beta} \right) \tag{6.7.7}$$

$$+ N_1 \left( \frac{2 N_2 \theta + P_2 \alpha z}{D_1 z} \right) + P_1 \left( -\frac{D_{12} G_0 \alpha}{D_1^2 \beta} + \frac{G_0 \alpha_2}{D_1 \beta} + \frac{N_2 \alpha}{D_1} \right)$$

$$+ M_1 \left( \frac{D_{12} v}{D_1^2} - \frac{v_2}{D_1} \right) - D_2 M_1 - D_1 M_2$$

$$S_{3,3} = -\,D_2 P_1 - D_1 P_2 \tag{6.7.8}$$

$$S_{3,4} = N_1 \left( \frac{D_{22} F_0 \beta}{D_2^2 \alpha} - \frac{F_0 \beta_2}{D_2 \alpha} + \frac{G_0 \beta_2 \theta}{D_2 z \alpha \beta} - \frac{D_{22} G_0 \theta}{D_2^2 z \alpha} - \frac{P_2 \beta}{D_2} \right) \tag{6.7.9}$$

$$+ P_1 \left( -\frac{G_0 \beta_2}{D_2 \beta} - \frac{N_2 \beta}{D_2} \right) + \frac{D_{22} Q_1 v}{D_2^2} - \frac{Q_1 v_2}{D_2} - D_2 Q_1 - D_1 Q_2$$

For systems A-C, the composite operator is

$$L_c \equiv \frac{F_0 \beta N_i}{D_2 \alpha} + \frac{D_0^2 v^2 \beta N_i}{D_2 G_0 \alpha} + \frac{D_0^3 v \beta N_i}{G_0 \alpha} + \frac{D_1 D_0^3 v \beta N_i}{D_2 G_0 \alpha}$$
$$- \frac{G_0 \theta N_i}{D_2 z \alpha} + \frac{D_1 D_0^4 \beta N_i}{G_0 \alpha} - \frac{D_0 v \theta N_i}{D_2 z \alpha} - \frac{D_0^2 \theta N_i}{z \alpha}$$

(6.7.10)

For systems A-C, the composite source is

$$\Gamma_i \equiv \frac{v^2 \beta D_0 S_{i,1}}{D_2 G_0 \alpha} + \frac{v \beta D_0^2 S_{i,1}}{G_0 \alpha} + \frac{D_1 v \beta D_0^2 S_{i,1}}{D_2 G_0 \alpha} + \frac{D_1 v \beta D_0 S_{i,2}}{D_2 G_0 \alpha}$$
$$+ \frac{D_1 \beta D_0^3 S_{i,1}}{G_0 \alpha} + \frac{D_1 \beta D_0^2 S_{i,2}}{G_0 \alpha} + \frac{v S_{i,3}}{D_2} + D_0 S_{i,3} + S_{i,4}$$
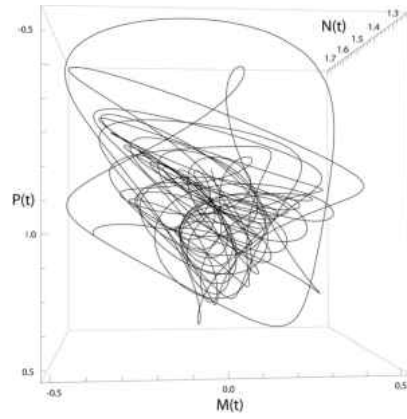
(6.7.11)

Figure 6.8: The stable quasiperiodic orbit created at line L3 has become unstable after the secondary Hopf bifurcation at L5.

# LIST OF REFERENCES

[1] V.K. Melnikov. On the stability of the center for time periodic perturbations. *Trans. Moscow Math. Soc.*, 12:1–57, 1963.

[2] L.M. Perko. *Differential Equations and Dynamical Systems.* Springer-Verlag, 2001.

[3] K. Huseyin. *Multiple Parameter Stability Theory and Its Applications.* Clarendon, 1986.

[4] J. Planeaux. *Bifurcation Phenomena in CSTR Dynamics.* PhD thesis, University of Minnesota, 1993.

[5] Jian-Qiao Sun and Albert C.J. Luo, editors. *Bifurcation and Chaos in Complex Systems, Pei Yu.* Elsevier, 2006.

[6] Y. Chen B. Liu and H. Zhang. Traveling wave solutions for generalized pochammer-chree equations. *Z. Naturforsch.*, 57a:874–882, 2002.

[7] X. Runzhang. Initial boundary value problem of two classes of evolution equations. *Fifth IMACS Conference on Nonlinear Evolution Equations*, 2007. (Submitted to Math. and Computers in Simulations).

[8] Z. Weiguo and W. X.Ma. Explicit solitary-wave solutions to generalized pochammer-chree equations. *Appl. Math. and Mech.*, 20:666–674, 1999.

[9] I. L. Bogolubsky. Some examplesof inelastic soliton interaction. *Comp. Phys.*, 31:149–155, 1977.

[10] R. J. Le Veque P. A. Clarkson and R. Saxton. Solitary-wave interactions in elastic rods. *Stud. Appl. Math.*, 75:95–122, 1986.

[11] R. Saxton. Existence of solutions for a finite nonlinearly hyperelastic rod. *J. Math. Anal. Applics.*, 105:59–75, 1985.

[12] D. J. Kaup and T. K. Vogel. Localized solutions for 1-d longitudinal wave propagation in microstructured solids. (To be submitted).

[13] G. B. Whitham. *Linear and Nonlinear Waves*. Wiley, 1975.

[14] A. Salupere, K. Tamm, and J. Engelbrecht. Interaction of solitary deformation waves in microstructured solids. *Proc. of 5th Intl. Conf. on Nonlin. Wave Equations, Athens, Georgia*, April 2007.

[15] J. Engelbrecht and F. Pastrone. Waves in microstructured solids with nonlinearities in microscale. *Proc. Estonian Acad. Sci. Phys. Math.*, 52:12–20, 2003.

[16] J. Engelbrecht, A. Berezovski, F. Patrone, and M. Braun. Waves in microstructured materials and dispersion. *Phil. Mag.*, 85:4127–4141, 2005.

[17] J. Janno and J. Engelbrecht. Solitary waves in nonlinear microstructured materials. *J. Phys. A: Math. Gen.*, 38:5159–5172, 2005.

[18] J. Janno and J. Engelbrecht. An inverse solitary wave problem related to microstructured materials. *Inverse Problems*, 21:2019–2034, 2005.

[19] A. Salupere, K. Tamm, J. Engelbrecht, and P. Peterson. On interaction of deformation waves in microstructured solids. *Proc. Estonian Acad. Sci. Phys. Math.*, 2007.

[20] J. Engelbrecht, A. Berezovski, and A. Salupere. Nonlinear deformation waves in solids and dispersion. *Wave Motion*, 2007.

[21] T. Vogel. *Systemes evolutifs*. Gautier-Villars, Paris, 1965.

[22] M Ueno and R. Lang. Conditions for self-sustained pulsation and bistability in semiconductor lasers. *Journal of Applied Physics*, 58:1689–1692, 1985.

[23] X Wang, G Li, and Charles S. Ih. Microwave/millimeter-wave frequency sub-carrier lightwave modulations based on self-sustained pulsation of a laser diode. *J Lightwave Tech.*, 11:309–315, 1993.

[24] C. M. Bender and S. A. Orszag. *Advanced mathematical methods for scientists and engineers.* McGraw-Hill, New York, 1978.

[25] WH Press, BP Flannery, SA Teukolsky, and WT VetterLing. *Numerical recipes in C.* Cambridge: Cambridge University Press, 1988.

[26] A. H. Nayfeh and B. Balachandran. *Applied Nonlinear Dynamics.* Wiley-Interscience, 1995.

[27] P Grassberger and I Procaccia. Measuring the strangeness of strange attractors. *Physica D*, 9:189–208, 1983.

[28] JD Farmer, E Ott, and JA Yorke. The dimension of chaotic attractors. *Physica D*, 7:153–180, 1983.

[29] Y. Termonia and Z. Alexandrowicz. Fractal dimension of strange attractors from radius size of arbitrary clusters. *Phys Rev Lett*, 51:1265–1268, 1983.

[30] P Bergé, Y Pomeau, and C Vidal. *Order within chaos.* New York: Wiley, 1984.

[31] R Seydel. *From equilibrium to chaos.* New York: Elsevier, 1988.

[32] GL Baker and JP Gollub. *Chaotic dynamics.* Cambridge: Cambridge University Press, 1990.

[33] HDI Abarbanel, MI Rabinovich, and MM Sushchik. *Introduction to nonlinear dynamics for physicists.* Singapore: World Scientific, 1993.

[34] D Kincaid and W Cheney. *Numerical analysis.* Pacific Grove, CA: Brooks/Cole, 1991.

[35] AH Nayfeh and DT Mook. *Nonlinear Oscillations.* New York: Wiley, 1979.

[36] S. Krise and S. Roy Choudhury. Bifurcations and chaos in a predator-prey model with delay and a laser-diode system with self-sustained pulsations. *Chaos, Solitons and Fractals*, 16:59–77, 2003.

[37] J. M. Cushing. Integrodifferential Equations and Delay Models in Population Dynamics. In *Lecture Notes in Biomathematics*, volume 20. Berlin: Springer-Verlag, 1977.

[38] K. Smitalova and S. Sujan. *A Mathematical Treatment of Dynamical Models in Biological Science.* Ellis Horwood, New York, 1991. And references therein.

[39] N. MacDonald. Time Lags in Biological Models. In *Lecture Notes in Biomathematics*, volume 27. Berlin: Springer-Verlag, 1978.

[40] M. Farkas. Stable oscillations in a predator-prey model with time lag. *J Math Appl*, 102:175–88, 1984.

[41] H.T. Davis. *Introduction to Nonlinear Differential and Integral Equations*. Dover, New York, 1962.

[42] H. El-Owaidy and A. A. Ammar. Stable oscillations in a predator-prey model with time lag. *J Math Appl*, 130:191–99, 1988.

[43] J. Hale. *Theory of functional differential equations*. Springer-Verlag, Berlin, 1977.

[44] N. MacDonald. Time delay in predator-prey models. *Math. Biosciences*, 28:321–30, 1976.

[45] N. MacDonald. II. Bifurcation theory. *Biosciences*, 33:227–34, 1977.

[46] J. E. Marsden and M. McCracken. *The Hopf Bifurcation and Its Applications*. Springer-Verlag, New York, 1976.

[47] J. D. Murray. A prepattern formation mechanism for animal coat markings. *J. Theoret. Biol.*, 88:161, 1981.

[48] E. Roos. Predator-Prey Models with Distributed Delay. Master's thesis, University of Central Florida, Orlando, 1991.

[49] S. R. Choudhury. On bifurcations and chaos in predator-prey models with delay. *Chaos, Solitons and Fractals*, 2:393–409, 1992.

[50] A. Turing. The chemical basis of morphogenesis. *Phil. Trans. R. Soc. Lond. B*, 237:37–72, 1952.

[51] C. W. Wardlaw. Evidence relating to the diffusion-reaction theory of morphogenesis. *New Phytol.*, 54, 1955.

[52] H. G. Othmer and L. E. Scriven. Instability and dynamic pattern in cellular networks. *J. Theoret. Biol.*, 32:507, 1971.

[53] L. A. Segel and J. L. Jackson. Dissipative structure: an explanation and an ecological example. *J. Theoret. Biol.*, 37:545, 1972.

[54] A. Gierer. Generation of biological patterns and form. *Prog. Biophys. Molec. Biol.*, 27:1, 1981.

[55] A. Gierer and H. Meinhardt. A theory of biological pattern formation. *Kybernetic*, 12:30, 1972.

[56] H. Meinhardt. *Models of biological pattern formation*. Academic Press, 1982.

[57] M. I. Granero, A. Porati, and D. Zanacca. A bifurcation analysis of pattern formation in a diffusion governed morphogenic field. *J. Math. Biol.*, 4:21, 1977.

[58] J. P. Keener. Activators and inhibitors in pattern formation. *Stud. Appl. Math*, 59:1, 1978.

[59] L. A. Segel. *Taxes in ecology and cell biology.* Springer-Verlag, 1984.

[60] J. Smoler. *Shock waves and reaction-diffusion equations.* Springer-Verlag, Berlin, 1984.

[61] F. Rothe. *Global solutions of reaction-diffusion equations.* Springer-Verlag, Berlin, 1984.

[62] P. C. Fife. *Mathematical aspects of reacting and diffusing systems.* Springer-Verlag, New York, 1979.

[63] J. D. Murray. *Mathematical Biology.* Springer-Verlag, Berlin, 1989.

[64] M. Mimura and J. D. Murray. On a diffusive predator-prey model which exhibits patchiness. *J. The*, 75:249, 1978.

[65] J. Bard. A model for generating aspects of zebra and other mammalian coat patterns. *J. Theoret. Biol.*, 93:363, 1981.

[66] H. C. Schaller. *Neurohormones and their functions in hydra.* Plenum, London, 1982.

[67] J. D. Murray, P.K. Maini, and R. T. Tranquillo. Mechanochemical models for generating biological pattern and form. *Phys. Reports*, 59:171, 1988.

[68] S. A. Levin and L. A. Segel. Pattern generation in space. *SIAM Rev.*, 27:45, 1985.

[69] L. Edelstein-Keshet. *Mathematical models in biology*. Random House, New York, 1988.

[70] Stefan C. Mancas and S. Roy Choudhury. Periodic and chaotic traveling wave patterns in reaction-diffusion/predator-prey models with general nonlinearities. *Far E. J. Dyn. Sys.*, 11:117–142, 2009.